

PHOTOELECTRIC DRIVEN DECOMPOSITION OF URACIL VIA HARD X-RAY
IRRADIATION

By

Trimaan Malik

Bachelor of Science - Physics
University of Nevada, Las Vegas
2018

A thesis submitted in partial fulfillment
of the requirements for the

Master of Science – Physics

Department of Physics and Astronomy
College of Sciences
The Graduate College

University of Nevada, Las Vegas
May 2024



Thesis Approval

The Graduate College
The University of Nevada, Las Vegas

May 1, 2024

This thesis prepared by

Trimaan Malik

entitled

Photoelectric Driven Decomposition of Uracil via Hard X-Ray Irradiation

is approved in partial fulfillment of the requirements for the degree of

Master of Science - Physics
Department of Physics and Astronomy

Michael Pravica, Ph.D.
Examination Committee Chair

Ashkan Salamat, Ph.D.
Examination Committee Member

Jason Steffen, Ph.D.
Examination Committee Member

Satish Bhatnagar, Ph.D.
Graduate College Faculty Representative

Alyssa Crittenden, Ph.D.
*Vice Provost for Graduate Education &
Dean of the Graduate College*

ABSTRACT

Radiation damage into biological samples creates substantial challenges across a wide range of fields, from biochemistry to materials science. This comprehensive study investigates the effects of x-ray irradiation on uracil, the only nucleobase exclusive to Ribonucleic acid (RNA), to understand how doping with 10% (by mass) of specific powdered elements impacts the sustained radiation damage. The experiments were conducted at the Brockhouse Undulator Beamline of the Canadian Light Source synchrotron. Virgin and doped uracil samples were irradiated with hard x-rays, above their respective absorption edges, and studied with x-ray diffraction to compare their decomposition behaviors. The Uracil reflections on the x-ray diffraction plots showed signs of radiation damage, increasing d-spacing and decreasing intensities, after extended irradiation. The decomposition yield was plotted against irradiation time and fit with a modified Avrami equation. This regression analysis revealed the linear nature of the radiation damage, with the decomposition yield of the doped samples growing faster compared to virgin uracil. This accelerated damage is attributed primarily to the photoelectric effect in the powdered dopants, where the absorption of x-ray photons above the electron binding energy leads to the emission of electrons and characteristic x-rays which bombard the uracil crystal structure and enhance the radiation damage. These findings offer insights into the effect elemental doping has on the stability of biological samples when exposed to hard x-rays as a method initiate and accelerate radiation damage.

ACKNOWLEDGMENTS

I would like to thank Dr. Michael Pravica, Dr. Jason Steffen, Dr. Ashkan Salamat, and Dr. Satish Bhatnagar for their mentorship and guidance. I wish to acknowledge Petrika Cifligu and Dr. Egor Evlyukhin for teaching me everything regarding sample preparation and conducting these experiments. I thank the staff at Canadian Light Source (Beatriz Moreno, Narayan Appathurai, Al Rahemtulla, and Joel Reid) for guiding me through setting up the experiments and collecting data. I also thank my family for supporting me throughout my entire life.

To my progenitors, in this timeline and the next.

TABLE OF CONTENTS

ABSTRACT.....	iii
ACKNOWLEDGMENTS	iv
TABLE OF CONTENTS.....	vi
LIST OF TABLES	viii
LIST OF FIGURES	ix
CHAPTER 1: INTRODUCTION	1
CHAPTER 2: BACKGROUND.....	3
2.1: Electromagnetic Waves.....	3
2.2: Inner Shell Chemistry	6
2.3: X-ray Absorption Spectroscopy	9
2.4: Crystallography	11
2.5: X-ray Diffraction.....	13
CHAPTER 3: SYNCHROTRON	17
3.1: Particle Accelerator	17
3.2: Beamline Setup	21
CHAPTER 4: EXPERIMENT	25
4.1: Sample Preparation	25
4.2: Data Processing	29
CHAPTER 5: RESULTS and DISCUSSION.....	34
5.1: Gold.....	34
5.2: Selenium.....	39
5.3: Niobium.....	43
5.4: Discussion	47

CHAPTER 6: CONCLUSION	50
APPENDIX.....	52
WORKS CITED	55
CURRICULUM VITAE.....	58

LIST OF TABLES

Table 1: Table of crystal structures and their parameters with their Bravais lattices.....	11
Table 2: Uracil parameters including crystal structure, axial lengths, axial angles, and Bravais lattice.....	30
Table 3: Modified Avrami fit parameters from (Fig. 19).....	35
Table 4: Modified Avrami fit parameters from (Fig. 21).....	36
Table 5: Modified Avrami fit parameters from (Fig. 23).....	38
Table 6: Modified Avrami fit parameters from (Fig. 25).....	40
Table 7: Modified Avrami fit parameters from (Fig. 27).....	42
Table 8: Modified Avrami fit parameters from (Fig. 29).....	44
Table 9: Modified Avrami fit parameters from (Fig. 31).....	46

LIST OF FIGURES

Figure A: Figure of RNA with the included nucleobases.....	1
Figure 1: Visual representation of the perpendicular nature of electric and magnetic fields (NASA et al., 2021a).....	3
Figure 2: The electromagnetic spectrum (NASA et al., 2021b).	6
Figure 3: Bohr atom model features the photoelectric effect with an ejection of a K-shell electron. As the vacancy is filled, characteristic x-rays are emitted (Rebollo, 2019).....	8
Figure 4: X-ray absorption plot with the EXAFS region highlighted. The sharp spike in absorption refers to the absorption edge (Sjöstedt, 2012).....	10
Figure 5: Several types of Bravais lattices (Rath, 2016).	12
Figure 6: Illustration on Bragg's law.....	14
Figure 7: Dioptas® software with the image of the Debye-Scherrer rings of Uracil at 14.5 keV and the corresponding XRD plot. The red overlay covers the shadows of the sample stage and beamstop to exclude them from the azimuthal integration.....	16
Figure 8: Schematic of the Canadian Light Source showing the path the electrons take in the synchrotron to the different beamlines (Cutler et al., 2017).	21
Figure 9: End station of the IVU beamline. (A) is the capillary tube in an aluminum holder on the sample stage. (B) is the beamstop to protect the detector (C) from stray x-rays that are not diffracted.	23
Figure 10: Radiation damage is characterized by decreased reflection intensities and unit cell expansion.	24
Figure 11: Mortar and pestle used for grinding.	26
Figure 12: Capillary tube with a 90% Uracil + 10% Niobium sample.....	26

Figure 13: Disassembled diamond anvil cell.....	27
Figure 14: View of the culet in the closed cell with a microscope with the sample powder (90% Uracil + 10% Selenium) covering most of the culet.....	28
Figure 15: Assembled diamond anvil cell.....	29
Figure 16: Uracil molecule from CrystalMaker software.....	30
Figure 17: Uracil XRD plot at 19.8 keV. The boxed peak has miller indices of (0 0 1) and was chosen for data analysis from every XRD image.	32
Figure 18: Uracil unit cell from VESTA. The lattice plane of miller indices (0 0 1) is highlighted in red.	33
Figure 19: Plot and fit of doped uracil sample at 14.5 keV with modified Avrami equation fit results.....	34
Figure 20: Initial and final uracil peak overlayed from the doped sample at 14.5 keV.....	35
Figure 21: Plot and fit of a pure uracil sample at 14.5 keV with the modified Avrami equation results.....	36
Figure 22: Initial and final uracil peak overlayed from the virgin uracil sample at 14.5 keV.....	37
Figure 23: Plot and fit of a doped uracil sample at 15.7 keV with the modified Avrami equation results.....	38
Figure 24: Initial and final uracil peak overlayed from the doped uracil sample at 15.7 keV.....	39
Figure 25: Plot and fit of a doped uracil sample in the DAC at 12.721 keV with the modified Avrami equation results.	40
Figure 26: Initial and final uracil peak overlayed from the doped uracil sample in the DAC at 12.721 keV.....	41

Figure 27: Plot and fit of a pure uracil sample in the DAC at 12.721 keV with the modified Avrami equation results.	42
Figure 28: Initial and final uracil peak overlayed from the pure uracil sample in the DAC at 12.721 keV.	43
Figure 29: Plot and fit of a pure uracil sample in the at 19.581 keV with the modified Avrami equation results.	44
Figure 30: Initial and final uracil peak overlayed from the pure uracil sample at 19.581 keV.....	45
Figure 31: Plot and fit of the doped uracil sample in the at 19.581 keV with the modified Avrami equation results.	46
Figure 32: Initial and final uracil peak overlayed from the doped uracil sample at 19.581 keV..	47
Figure 33: Damaged capillary tube. The damage caused slight discoloration.....	48
Figure 34: Mass energy-absorption coefficient for Gold as a function of the photon energy. The sharp increases in the coefficient represent the absorption edges (National Institute of Standards and Technology, 2004).	52
Figure 35: Spectrum of Gold's characteristic x-rays (XRF RESEARCH, 2024).	52
Figure 36: Mass energy-absorption coefficient for Selenium as a function of the photon energy. The sharp increases in the coefficient represent the absorption edges (National Institute of Standards and Technology, 2004).	53
Figure 37: Spectrum of Selenium's characteristic x-rays (XRF RESEARCH, 2024).	53
Figure 38: Mass energy-absorption coefficient for Niobium as a function of the photon energy. The sharp increases in the coefficient represent the absorption edges (National Institute of Standards and Technology, 2004).	54
Figure 39: Spectrum of Niobium's characteristic x-rays (XRF RESEARCH, 2024).	54

CHAPTER 1: INTRODUCTION

Radiation damage from x-rays has long been considered a nuisance in experiments conducted at synchrotrons and other x-ray sources for many decades. As these facilities produce extremely powerful x-rays, they have often compromised the original integrity of biological samples during studies. With the advent of the pandemic from the RNA-based COVID-19 virus, the goal of damaging RNA based samples with monochromatic x-rays was pursued by the Pravica Group. Utilizing the hard x-rays from synchrotrons to selectively decompose an RNA-based sample became the foundation for this project. RNA is one of the two main types of nucleic acids found within cells, with the other deoxyribonucleic acid (DNA) [Fig. A].

RNA

(Ribonucleic acid)

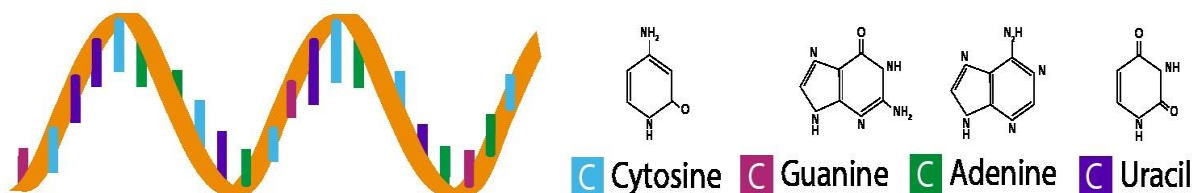


Figure A: Figure of RNA with the included nucleobases (National Genomics Education Programme, n.d.).

RNA is comprised of nucleotides that consist of a ribose sugar, a phosphate group, and one of four nucleobases: adenine, cytosine, guanine, and uracil. Furthermore, Uracil is the only nucleobase that is entirely found within RNA while the remaining three nucleobases also exist in DNA (Rosenberg, 1985). As the goal of these experiments was to only damage the RNA, targeting the uracil nucleobase exclusive to it was the optimal choice.

The fundamental question posed was whether adding small amount of elemental powder could enhance the x-ray induced decomposition of uracil by utilizing the photoelectric effect. As the photoelectric effect leads to the ejection of photoelectrons and the generation of characteristic x-rays, leveraging these phenomena to enhance the damage became the focus of the experiments. Uracil was doped with three different elements: gold, selenium, and niobium at 9:1 ratio by mass. The samples were irradiated with hard x-rays at an energy slightly above the absorption edge of the element, respectively. X-ray diffraction images were recorded periodically during irradiation and the uracil peak with the highest intensity from the diffraction plot was integrated to determine the area. These area values were used to formulate a decomposition yield to quantify the amount of uracil decomposition. After the decomposition yield was plotted as a function of irradiation time, a modified Avrami equation was fit to quantify the rate and behavior of the decomposition.

CHAPTER 2: BACKGROUND

2.1: Electromagnetic Waves

X-rays are a type of electromagnetic radiation, a form of energy that moves through space at the speed of light as waves. These waves consist of the electric (\vec{E}) and magnetic fields (\vec{B}) for particles that are perpendicular to one another [Fig. 1].

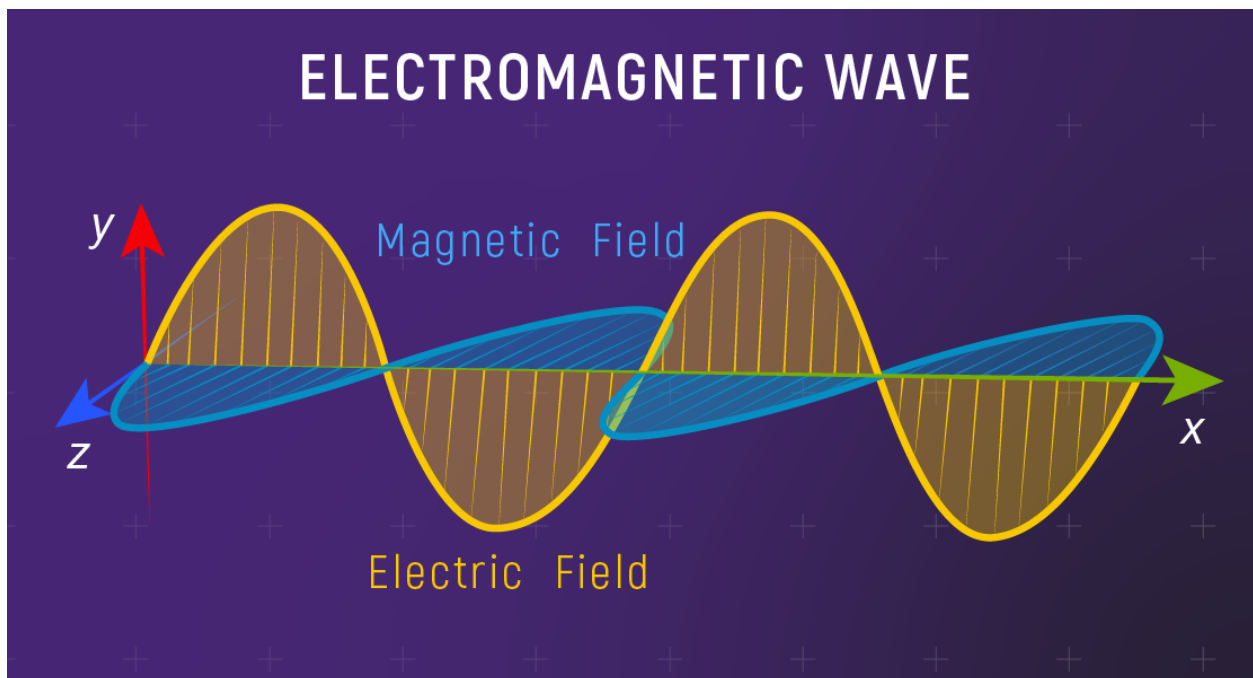


Figure 1: Visual representation of the perpendicular nature of electric and magnetic fields (NASA et al., 2021a).

The wavelength (λ) refers to the distance between the peaks of the wave and is expressed in the terms of energy using [Eq. 1] where E is energy, c represents the speed of light ($2.998 \times 10^{10} \frac{\text{cm}}{\text{s}}$), and h as Planck's constant ($6.626 \times 10^{-27} \text{ erg} \cdot \text{s}$):

$$E = \frac{hc}{\lambda} \quad \text{[Equation 1]}$$

The electromagnetic waves are governed by Maxwell's equations, developed by James Maxwell during the 19th century, which link the laws of electricity and magnetism [Eq. 2].

$$\nabla \cdot \vec{E} = 4\pi\rho \text{ (Gauss' Law)} \quad \text{[Equation 2.1]}$$

$$\nabla \cdot \vec{B} = 0 \text{ (Gauss' Law for Magnetism)} \quad \text{[Equation 2.2]}$$

$$\nabla \times \vec{E} = -\frac{1}{c} \frac{\partial \vec{B}}{\partial t} \text{ (Faraday's Law)} \quad \text{[Equation 2.3]}$$

$$\nabla \times \vec{B} = \frac{1}{c} \left(4\pi\vec{J} + \frac{\partial \vec{E}}{\partial t} \right) \text{ (Ampere's Law)} \quad \text{[Equation 2.4]}$$

This law relates the divergence of an electric field, at any point in space, to the charge density (ρ) [Eq. 2.1]. In terms of magnetism, Gauss' law implies that the divergence of a magnetic field is equal to zero in all cases and that magnetic monopoles do not exist [Eq. 2.2]. Faraday's law states that a rotating electric field is caused by a time-varying magnetic field. The negative sign indicates the electric field opposes the change in magnetic field [Eq. 2.3]. Ampere's Law, with the addition of the displacement current, states that a circulating magnetic field is influenced by both the conduction current and the changing electric field [Eq. 2.4]. However, in terms of electromagnetic waves, Maxwell's equations are "source-free" as waves can propagate through free space without charges ($\rho = 0$) or currents ($\vec{J} = 0$) [Eq. 3] (Fitzpatrick, 2008).

$$\nabla \cdot \vec{E} = 0 \quad \text{[Equation 3.1]}$$

$$\nabla \cdot \vec{B} = 0 \quad [\text{Equation 3.2}]$$

$$\nabla \times \vec{E} = -\frac{1}{c} \frac{\partial \vec{B}}{\partial t} \quad [\text{Equation 3.3}]$$

$$\nabla \times \vec{B} = \frac{1}{c} \frac{\partial \vec{E}}{\partial t} \quad [\text{Equation 3.4}]$$

These equations describe the electric and magnetic fields as coupled, where \vec{E} becomes a source for \vec{B} and vice versa, which can then be used to derive the wave equation (Eq. 4.1):

$$\nabla \times (\nabla \times \vec{E}) = \nabla \times \left(-\frac{1}{c} \frac{\partial \vec{B}}{\partial t} \right) \quad [\text{Equation 4.1}]$$

$$\nabla \times \nabla \times \vec{E} = \nabla(\nabla \cdot \vec{E}) - \nabla^2 \vec{E} = -\nabla^2 \vec{E} \quad [\text{Equation 4.2}]$$

$$-\nabla^2 \vec{E} = \nabla \times \left(-\frac{1}{c} \frac{\partial \vec{B}}{\partial t} \right) = -\frac{1}{c} \frac{\partial}{\partial t} (\nabla \times \vec{B}) = -\frac{1}{c^2} \frac{\partial^2 \vec{E}}{\partial t^2} \quad [\text{Equation 4.3}]$$

$$c^2 \nabla^2 \vec{E} = \frac{\partial^2 \vec{E}}{\partial t^2} \quad [\text{Equation 4.4}]$$

The derivation is for the electric field wave equation and can also be applied to calculate the magnetic field wave equation (Eq. 4.2):

$$c^2 \nabla^2 \vec{B} = \frac{\partial^2 \vec{B}}{\partial t^2} \quad [\text{Equation 4.5}]$$

(Eq. 4.1) and (Eq. 4.2) argue that the electric field time derivative is impacted by the field's variations in space (Hughes, 2005). Changes within an electric field create changes within the magnetic field and vice versa, providing the foundation for the movement of electromagnetic radiation as waves [Fig. 2].

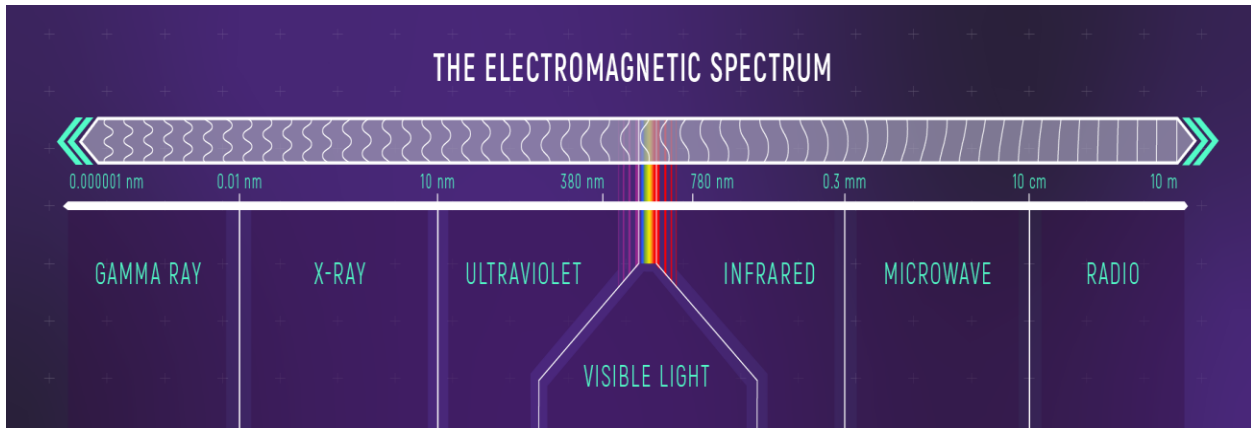


Figure 2: The electromagnetic spectrum (NASA et al., 2021b).

2.2: Inner Shell Chemistry

When X-rays move through matter, they interact with the atoms and molecules present.

The x-ray photons are absorbed by the atoms and/or molecules and cause the ejection or photoelectric absorption of an inner-shell electron. Inner-shell electrons are the electrons that are closest to the nucleus of the atom. These ejected electrons are known as photoelectrons and are created when the energy of the x-ray photon is greater than or equal to the electron binding energy, the minimum energy required to ionize electrons. The kinetic energy of a photoelectron is expressed using Planck's formula (Eq. 1) and the binding energy (E_B) (Eq. 5):

$$KE_{photoelectron} = \frac{hc}{\lambda} - E_B \quad [\text{Equation 5}]$$

Inner-shell electrons are tightly bound to the nucleus because of the strong Coulombic attraction to the positively charged protons within the nucleus. Furthermore, these electrons are organized in shells including the K-shell ($n = 1$), L-shell ($n = 2$), and M-shell ($n = 3$) with n being the shell quantum number. As the K-shell electrons are closest to the nucleus, they are in the lowest energy state whereas the M-shell electrons are in a higher energy state as they are farther away (Piróth & Sólyom, 2007). A different maximum number of electrons can occupy these shells: two electrons for the K-shell (1s), eight electrons in the L-shell (2s 2p), and eighteen electrons for the M-shell (3s 3p 3d). The K-shell can only hold two electrons whereas the other shells can contain subshells to accommodate for atoms with a higher number of electrons as each subshell has a maximum number of electrons can hold and can have slightly different energies. These limitations are governed by the Pauli Exclusion Principle that stipulates that no two electrons exist in the same state, having the same quantum numbers (Crasemann, 2012).

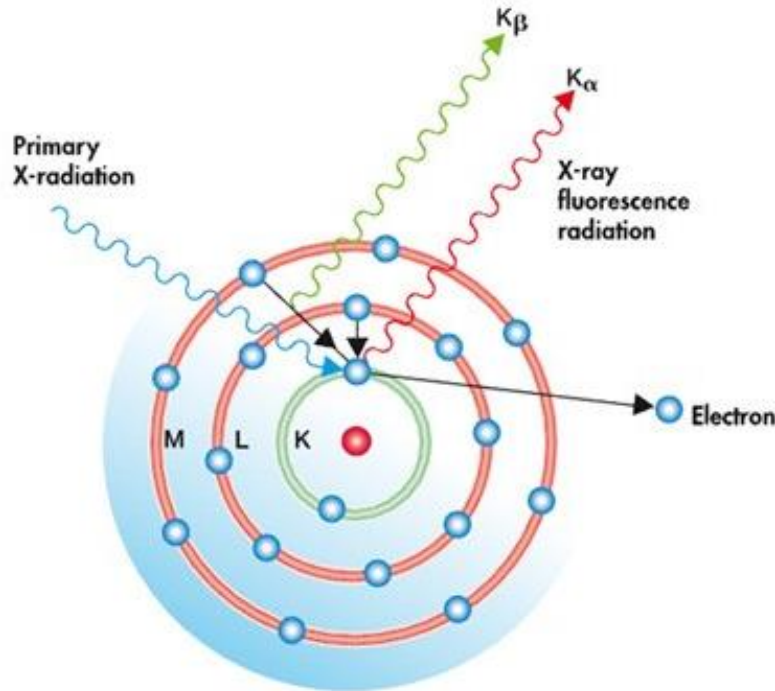


Figure 3: Bohr atom model features the photoelectric effect with an ejection of a K-shell electron. As the vacancy is filled, characteristic x-rays are emitted (Rebollo, 2019).

Once an electron is ejected and a vacancy is created, the atom becomes unstable. To promote stability, vacancies are filled with an electron from a higher energy state. The relaxation to a lower energy state releases energy and either leads to characteristic x-ray emission or Auger electron emission. In the characteristic x-ray emission, an x-ray photon is released with an energy equal to the difference in binding energy between the two shells or subshells. If a K-shell electron is ejected and the vacancy is filled with an electron from the L-1 shell, the characteristic x-ray emitted is notated as $K\alpha_1$ where the first letter denotes the location of the vacancy (West, 1991). Since the L-shell is the next outermost shell, it is denoted as α with “1” representing the subshell. Likewise, if the electron comes from the L-2 shell it will emit a $K\alpha_2$ characteristic Xray [Fig. 3]. Therefore, heavier atoms with more electrons emit more characteristic x-rays as there are more locations for relaxation and transition. Furthermore, the emitted energy is used to

identify the atoms in an arrangement and quantify their concentrations as each element has a different number of electrons. In the case of an Auger electron, the energy difference is transferred to another outer shell electron that is then emitted from the atom (Jensen, 2017).

2.3: X-ray Absorption Spectroscopy

The probability of the x-rays being absorbed is described with Beer's Law with the initial or incident intensity (I), intensity through the sample or transmitted (I_0), sample thickness (t), and the absorption coefficient (μ) (Eq. 6.1).

$$I = I_0 e^{-\mu t} \quad \text{[Equation 6.1]}$$

Samples can either be solid, liquid, or gas. Furthermore, the absorption coefficient is a function of the sample density (ρ), atomic number (Z), atomic mass (M), and the x-ray energy (E) (Eq. 6.2).

$$\mu \approx \frac{\rho Z^4}{ME^3} \quad \text{[Equation 6.2]}$$

A strong increase in absorption occurs when the x-ray photon's energy is equal to the binding energy of an inner shell, which corresponds to an absorption edge. The absorption coefficient (Eq. 6.2) is analyzed as a function of energy with X-ray Absorption Fine Structure (XAFS). XAFS consists of two separate techniques: X-ray Absorption Near Edge Structure (XANES) and Extended X-ray Absorption Fine Structure (EXAFS). XANES focuses on energies about 30 eV just above the absorption edge whereas EXAFS corresponds with changes well

above the absorption edges. XAFS plots show the relationship between an increasing energy level and $\mu(E)$, the absorption coefficient in transmission (Eq. 6.3) (Evans, 2017).

$$\mu(E) = \ln\left(\frac{I_0}{I}\right) \quad \text{[Equation 6.3]}$$

The transmission method of measurement occurs when detectors are placed before and after the sample to measure the number of x-rays transmitted. When the respective intensities are measured, (Eq. 6.3) is utilized to calculate the absorption as a function of the x-ray intensity which leads to the discovery of absorption edges (Bunker, 2010).

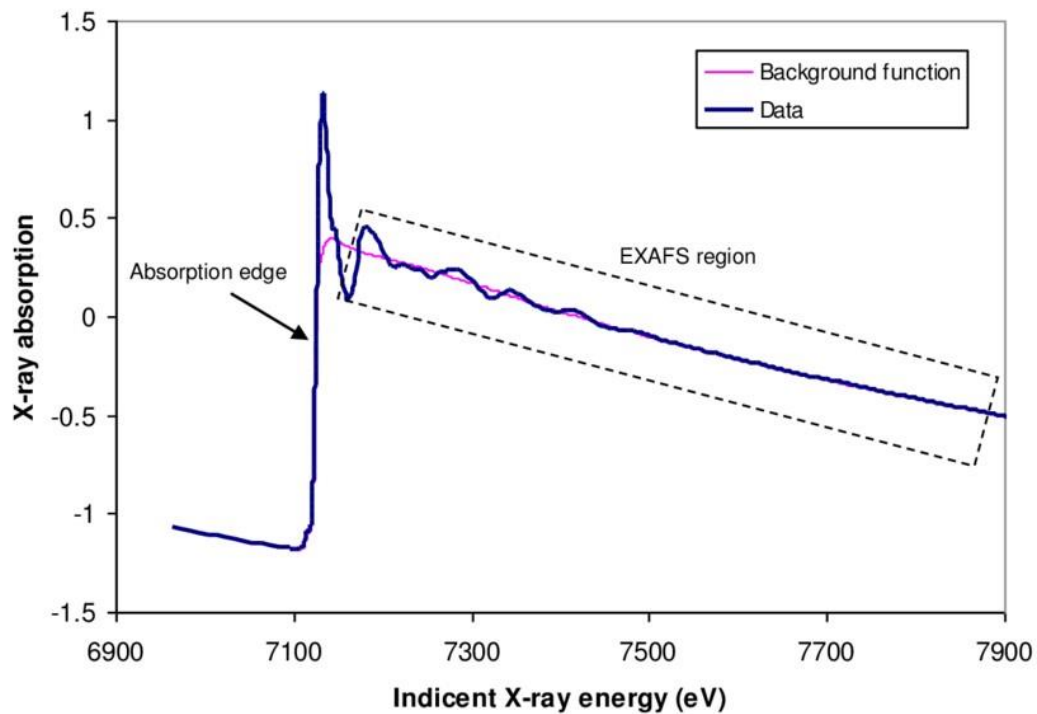


Figure 4: X-ray absorption plot with the EXAFS region highlighted. The sharp spike in absorption refers to the absorption edge (Sjöstedt, 2012).

2.4: Crystallography

A Bravais lattice refers to the periodic array in which atoms occupy a crystal structure with translational symmetry [Fig. 4]. Specifically, it is an infinite array of points where the orientation and arrangement does not change regardless of the point of view. In three dimensions, the lattice translation vector are represented with position vectors R , n being any integer, and \vec{a} as primitive vectors that exist in different directions [Eq. 7] (Hammond, 2001).

$$\vec{R} = n_1\vec{a}_1 + n_2\vec{a}_2 + n_3\vec{a}_3 \quad \text{[Equation 7]}$$

With full symmetry, a Bravais lattice can have fourteen distinct space groups that lead to seven crystal systems which make up the unit cell. The translational symmetry of the lattices is categorized in four ways: primitive, body-centered, face-centered, and base-centered. The three vectors that symbolize the edge of the cell (a , b , c) are the axial lengths. Similarly, the angles between those vectors (α , β , γ) are the axial angles.

System	Axial Length	Axial Angle	Bravais Lattice
Cubic	$a = b = c$	$\alpha = \beta = \gamma = 90^\circ$	Primitive, Body-centered, Face-centered
Tetragonal	$a = b \neq c$	$\alpha = \beta = \gamma = 90^\circ$	Primitive, Body-centered
Orthorhombic	$a \neq b \neq c$	$\alpha = \beta = \gamma = 90^\circ$	Primitive, Body-centered, Face-centered
Rhombohedral (Trigonal)	$a = b = c$	$\alpha = \beta = \gamma \neq 90^\circ$	Primitive
Hexagonal	$a = b \neq c$	$\alpha = \beta = 90^\circ, \gamma = 120^\circ$	Primitive
Monoclinic	$a \neq b \neq c$	$\alpha = \gamma = 90^\circ; \beta \neq 90^\circ$	Primitive, Base-centered
Triclinic	$a \neq b \neq c$	$\alpha \neq \beta \neq \gamma$	Primitive

Table 1: Table of crystal structures and their parameters with their Bravais lattices.

Miller indices are a notation system used for crystal structures to describe their planes and directions. The reciprocal of the x, y, and z points where the plane intercepts, multiplied by the least common factor, leads to whole numbers that are the miller indices (h, k, l). However, if the plane is parallel to an axis, the associated miller index is 0 (Suryanarayana & Norton, 2013).

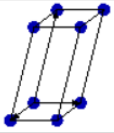
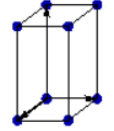
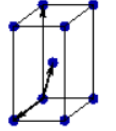
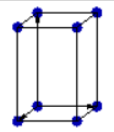
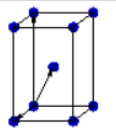
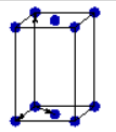
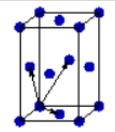
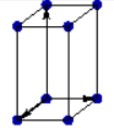
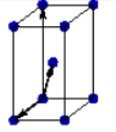
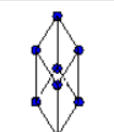
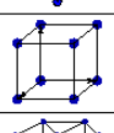
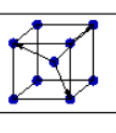
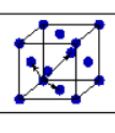
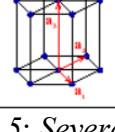
Simple (P)	Volume centered (I)	Base centered (C)	Face centered (F)
			
			
			
			
			
			
			

Figure 5: Several types of Bravais lattices (Rath, 2016).

2.5: X-ray Diffraction

Bragg's law provides a foundation for the interaction between the crystal structures and the diffracted x-rays. When monochromatic x-rays are directed at a crystal, the waves interact with the atoms and cause elastic scattering. This type of scattering conserves the frequency or energy of the x-rays and reflects secondary waves. These reflected waves interfere constructively with one another, generating a diffraction pattern. Constructive interference occurs when the waves diffracted from the crystal synchronize, matching up crest to crest or trough to trough. With wavelength λ , d-spacing d (distance between lattice planes), angle of diffraction θ , order of diffraction n , Bragg's law is represented by [Eq. 8.1]. However, n is typically set to one for simplicity and that the first-order reflection has the highest intensity (He, 2018).

$$n\lambda = 2d \sin \theta$$

[Equation 8.1]

Bragg's Law

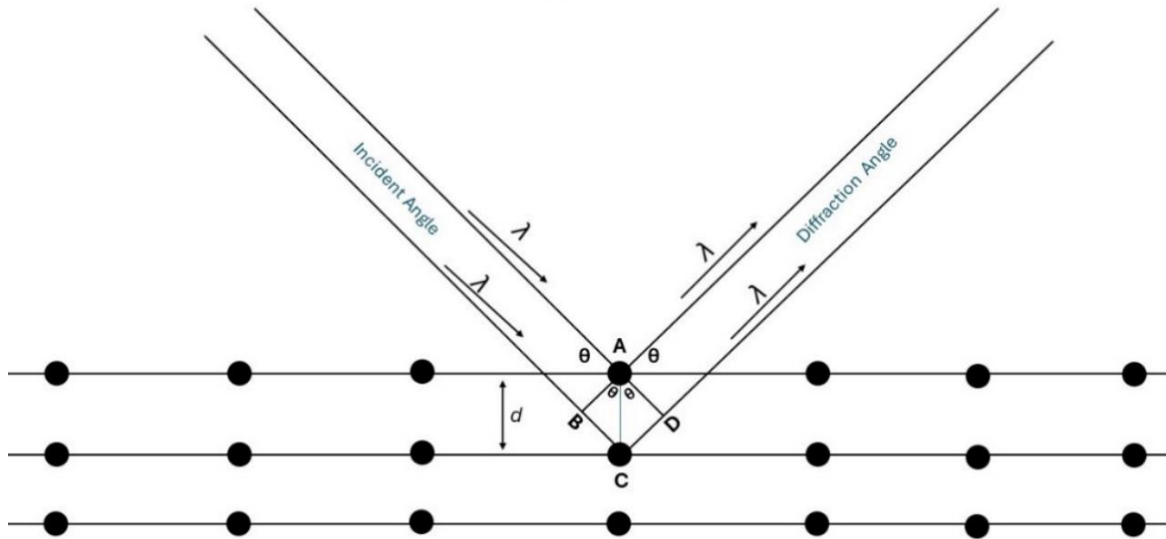


Figure 6: Illustration on Bragg's law.

The equation is derived from simple trigonometry [Fig. 6].

$$BC = CD \quad \text{[Equation 8.2]}$$

$$n\lambda = BC + CD \quad \text{[Equation 8.3]}$$

$$n\lambda = 2BC \quad \text{[Equation 8.4]}$$

$$BC = d \sin \theta \quad \text{[Equation 8.5]}$$

$$n\lambda = 2d \sin \theta \quad \text{[Equation 8.1]}$$

Bragg's law [Eq. 8.1] is rearranged to solve for the d-spacing [Eq. 9.1]:

$$\lambda = 2d \sin \theta \quad \text{[Equation 9.1]}$$

$$\frac{\lambda}{2 \sin \theta} = d \quad \text{[Equation 9.2]}$$

Powder samples are made of highly ordered crystallites that are positioned in random directions. The random orientation of these grains ensures that all lattice planes are present, but only a small amount are oriented correctly to satisfy Bragg's law and diffract. When combined with the random orientations of the grains, x-rays diffract into a cone shape for each d-spacing to produce images of Debye-Scherrer rings. Furthermore, each ring represents a set of crystallographic planes from the crystal structure and undergoes azimuthal integration to generate x-ray diffraction plots (Pahuja, 2005).

Dioplas® software was an essential part of this project, providing a simple platform to integrate the 2D x-ray diffraction scans into Intensity vs. 2θ diffraction plots. The program incorporates pyFAI (Python Fast Azimuthal Integration), a Python library for azimuthal integration of diffraction images (Prescher & Prakapenka, 2015). This type of integration translates the Debye-Scherrer rings (2D) into an x-ray diffraction plot (1D), a graph that displays the intensity of the diffracted x-rays as a function of the diffraction angle (2θ) [Fig. 7]. The rings are represented by peaks in intensity at specific angles, showing the location of the crystallographic planes.

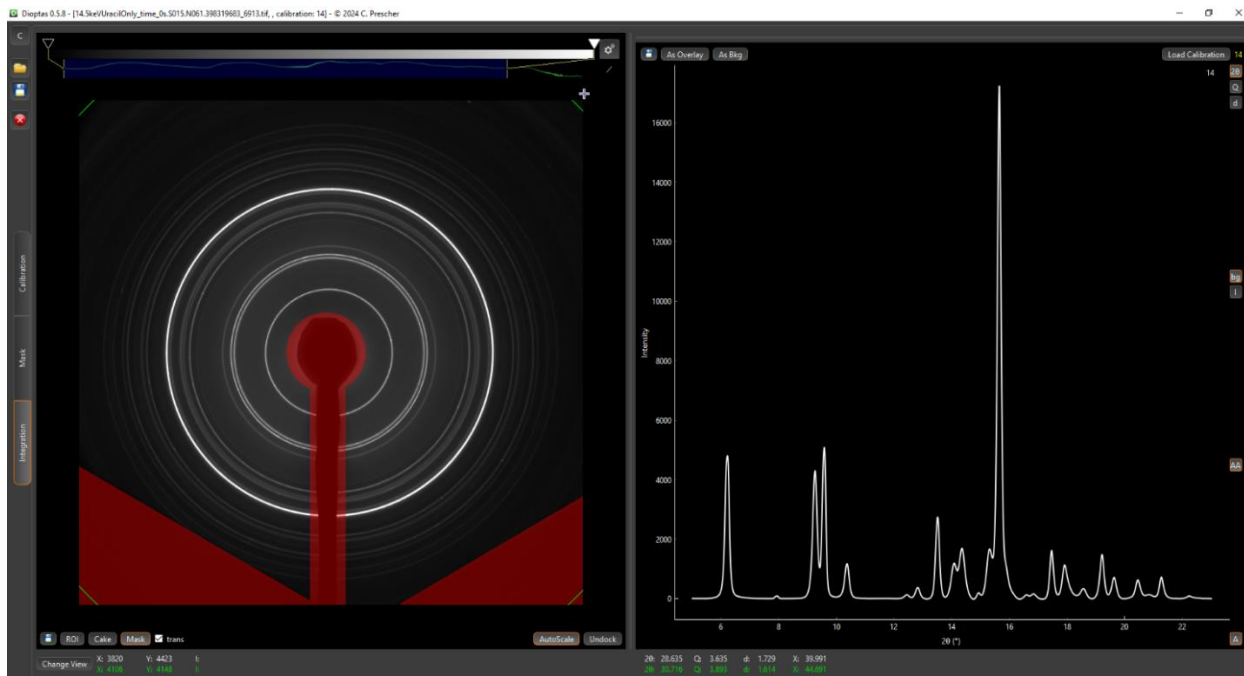


Figure 7: Dioptas® software with the image of the Debye-Scherrer rings of Uracil at 14.5 keV and the corresponding XRD plot. The red overlay covers the shadows of the sample stage and beamstop to exclude them from the azimuthal integration.

More intense and sharper peaks correspond to more degrees of ordered crystallinity within the material, indicating a highly ordered arrangement of atoms which leads to more constructive interference. Every x-ray diffraction scan has an inherent background signal that arises from stray x-rays, air scattered x-rays, or fluorescence from the sample holder itself. Therefore, background subtraction is often the first step in data treatment as it isolates the peaks of the crystal structure and improves the baseline by bringing it closer to the 2θ axis (Egami & Billinge, 2003).

CHAPTER 3: SYNCHROTRON

3.1: Particle Accelerator

As these x-ray experiments required a tremendous amount of energy (> 7 keV), focusing, and tunability, the work was conducted at the Canadian Light Source synchrotron in Saskatoon, Saskatchewan, Canada using the Brockhouse Undulator Beamline (IVU). A synchrotron is a type of particle accelerator that pushes a beam of charged particles to speeds just under the speed of light. These facilities are desirable for ultraviolet, infrared, and x-ray experiments as they provide a high amount of flux, brightness, and photon energies (Fodje et al., 2020). Fundamentally, a synchrotron takes advantage of centripetal forces and magnetic fields to operate. This force is described in [Eq. 10] with centripetal force F_c , mass m , velocity v , and radius r :

$$F_c = \frac{mv^2}{r} \quad \text{[Equation 10]}$$

When the charged particle is moving through the magnetic field, the force works perpendicular to the direction of the traveling particle and the direction of the field itself. Additionally, the magnetic field bends the path of the charged particle (Codling et al., 2013).

The movement of the particle is explained with Lorentz force law which defines a relationship between force (\vec{F}), charge (q), velocity (\vec{v}), electric field (\vec{E}), and magnetic field (\vec{B}) [Eq. 11.1]:

$$\vec{F} = q \left(\vec{E} + \frac{\vec{v}}{c} \times \vec{B} \right) \quad \text{[Equation 11.1]}$$

As the magnetic field is perpendicular to the velocity, [Eq. 11.1] is simplified into [Eq. 11.2] in terms of the magnetic force for the circular motion:

$$F = \frac{q}{c} v B \quad [\text{Equation 11.2}]$$

This is equated to [Eq. 10] as the magnetic and centripetal forces must be equal to keep the particle in a circular motion [Eq. 12.1]:

$$\frac{mv}{r} = \frac{q}{c} B \quad [\text{Equation 12.1}]$$

Therefore, the radius of the circular path is solved [Eq. 12.2]:

$$\frac{cmv}{qB} = r \quad [\text{Equation 12.2}]$$

Furthermore, the time for a full rotation or period T is equal to the circumference divided by the velocity [Eq. 13.1]:

$$T = \frac{2\pi r}{v} \quad [\text{Equation 13.1}]$$

The radius r is replaced by [Eq. X] to calculate the period of the particle [Eq. 13.2]:

$$T = \frac{2\pi cm}{qB} \quad [\text{Equation 13.2}]$$

However, as the electron is moving at just below the speed of light, it is important to introduce the Lorentz factor γ to describe its relativistic behavior. As the particle is moving

incredibly fast, time moves slower for the electron than an outside observer (time dilation). Furthermore, the length of the electron appears shorter to the outside observer in the direction of its motion (length contraction) (Kogut, 2018). This phenomenon is known as time dilation and is represented using the Lorentz factor γ [Eq. 14].

$$\gamma = \left[1 - \left(\frac{v}{c} \right)^2 \right]^{-1} \quad \text{[Equation 14]}$$

For a synchrotron, $\gamma \gg 1$ to represent the existence of time dilation and length contraction. By considering [Eq. X], the total energy of the particle E_{total} is defined with its mass m , the speed of light c , and the Lorentz factor γ [Eq. 15] (Faraoni, 2013):

$$E_{total} = \gamma mc^2 \quad \text{[Equation 15]}$$

An electron gun is the source of electrons for a particle accelerator. A beam is produced by heating a cathode to overcome the work function, through thermionic emission, which are then accelerated by the anode. The work function is the minimum energy required to separate an electron from the material's surface with the temperature reaching around 1000 Celsius for thermionic emission. For CLS, their electron gun cathode is made from tungsten oxide. The current density (J) of thermionic emission, the current flowing per unit area, is represented by the Richardson-Dushman equation with temperature T , the work function W , the Boltzmann constant k (1.381×10^{-16} erg/K), and the Richardson constant A_0 1.2×10^6 A/m²K² [Eq. 16] (Chattopadhyay, 2006):

$$J = A_0 T^2 e^{-W/kT}$$

[Equation 16]

The particles from the electron gun travel to the linear accelerator (LINAC) and are accelerated to 99.9998% the speed of light with an energy of 250 MeV. Once the electrons are injected into the LINAC, they pass through radio frequency cavities. Within these metallic and hollow cavities, the electrons pass through radio frequency waves that generate electric fields and oscillate at 2,856 MHz. This interaction pushes the electrons into the direction of the electric fields to be accelerated into the booster ring (Wiedemann, 2013).

Like the LINAC, the booster ring uses radio frequency cavities at 500 MHz to further accelerate the electrons to 2900 MeV. These particles travel in a circular path and complete 1.5 million rotations in 0.6 seconds with the assistance of magnets. The electric fields of dipole and quadrupole magnets in the booster ring bend the path of the electrons which causes acceleration.

After reaching 2900 MeV, the electrons travel from the booster ring to the storage ring to circulate for 4-12 hours, repeating once per second for 600 cycles. Twelve straight sections consisting of dipole, quadrupole, and sextuple magnets bend the path of the particles for circulation. Within the storage ring the electrons produce synchrotron light, a type of electromagnetic radiation, which is sent to the beamline to conduct experiments (Canadian Light Source & University of Saskatchewan, n.d.-b) [Fig. 8]. As it spans a significant range of the electromagnetic spectrum, synchrotron light is used for numerous electromagnetic experiments. Furthermore, the radiation is extremely polarized and collimated which provides a highly focused and high flux beam (Willmott, 2019). Having a focused beam allows for the synchrotron light to be concentrated in a very small area. A beam with a higher flux translates to a more powerful beam, providing more photons per second for the area.

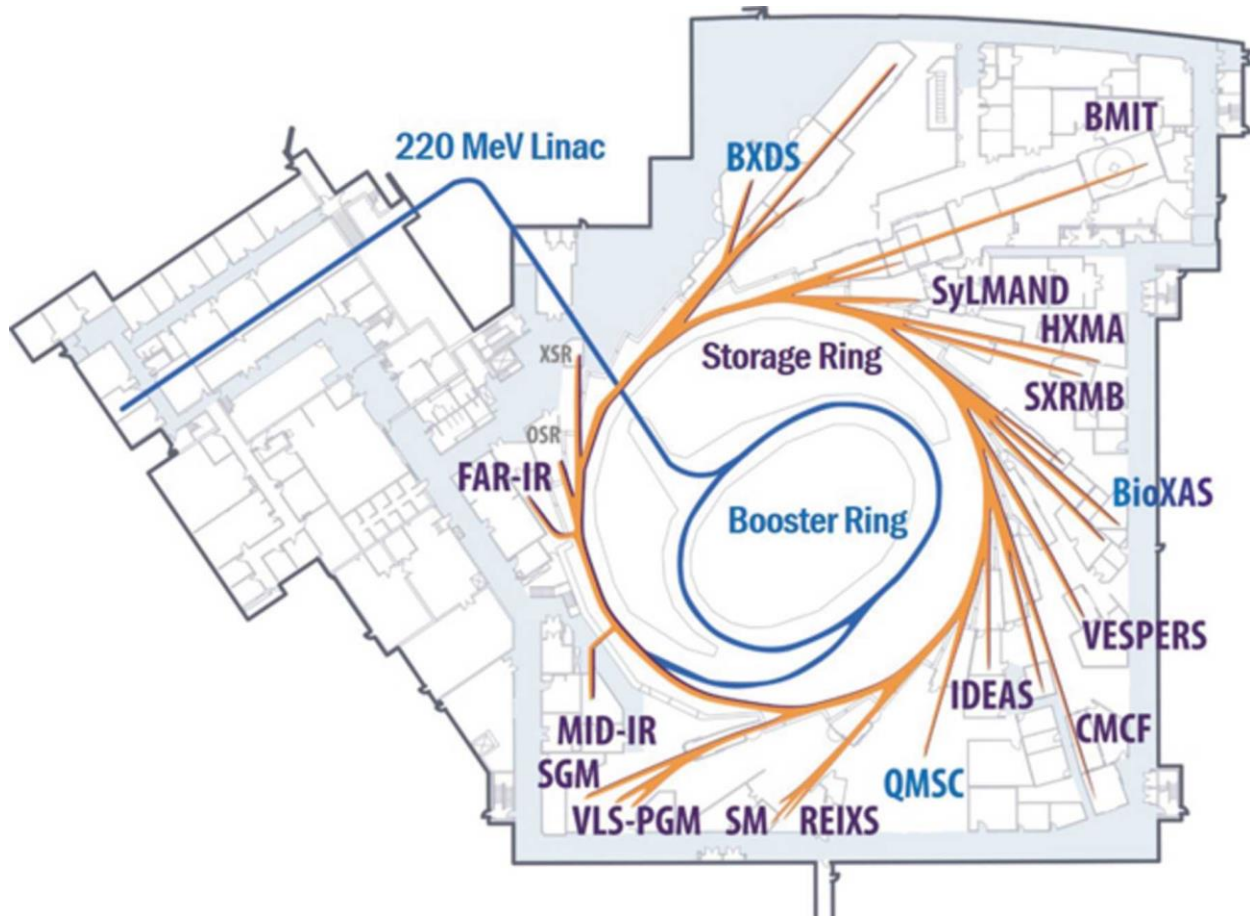


Figure 8: Schematic of the Canadian Light Source showing the path the electrons take in the synchrotron to the different beamlines (Cutler et al., 2017).

3.2: Beamline Setup

The experiments were conducted at the Canadian Light Source synchrotron in Saskatoon, Saskatchewan, Canada. Specifically, the experiments were completed at the Brockhouse Diffraction Sector Undulator beamline. This beamline provides an energy range between 5 keV to 24 keV from an in-vacuum undulator using odd harmonics 3rd to 11th. Harmonics represent integer multiples of the fundamental frequency of the synchrotron light. The heart of this beamline is the in-vacuum undulator (IVU) with a 20 mm period, Sm₂Co₁₇ permanent magnets, and poles made of pure iron. This component pushes the beam through a sinusoidally shifting

magnetic field, generated by the permanent magnets, which causes it to “wobble” and generate x-rays. The 20 mm period refers to the distance between the magnetic poles within the device. The next major component in the beamline is the multilayer monochromator that allows for a specific wavelength to be selected for the experiments. Consisting of thin layers of two different materials, the multilayer monochromator uses the constructive interference of the reflected waves from the x-ray beam to precisely generate a wavelength from the incident radiation. Before reaching the end station, the x-ray beam passes through the horizontal and vertical focusing mirrors that are slightly angled, with respect to the beam, to allow independent horizontal and vertical focusing. This enables the x-ray beam to be concentrated in a very small area to maximize the flux reaching the sample. For the IVU beamline, the flux values were $10^{12} \frac{\text{photons}}{\text{second}}$ (Diaz et al., 2014).

The end station consists of a vacuum tube, sample holder, beamstop, and diffractometer. As air molecules can scatter x-ray photons, adding a vacuum tube to the beam path reduces the air scattering. After the beam is absorbed by the sample, the diffraction rings are read by the diffractometer. Lastly, any stray x-ray photons are absorbed by the beamstop to protect the detector (Canadian Light Source & University of Saskatchewan, n.d.-a) [Fig. 9].

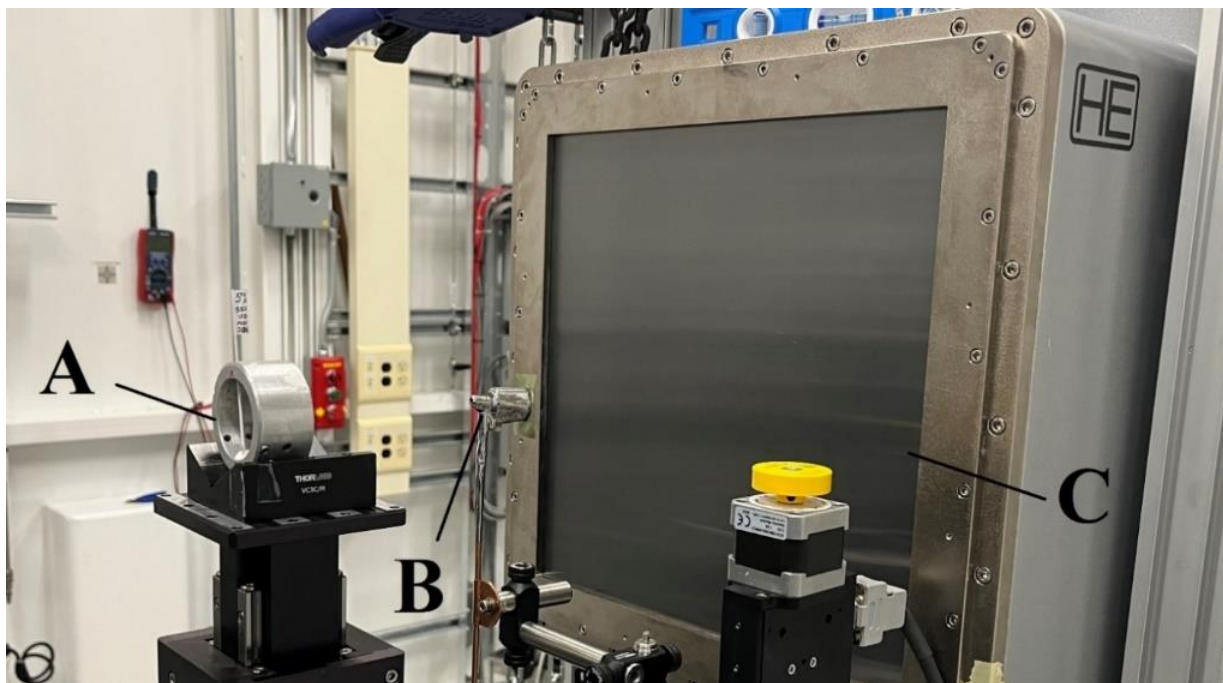
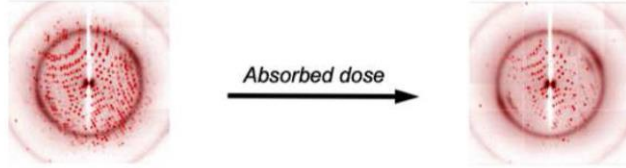


Figure 9: End station of the IVU beamline. (A) is the capillary tube in an aluminum holder on the sample stage. (B) is the beamstop to protect the detector (C) from stray x-rays that are not diffracted.

Any exposure to a high flux monochromatic x-ray beam has the potential to induce radiation damage, characterized by an increase in d-spacing and a decrease in intensity on the x-ray diffraction plot [Fig. 10]. As the sample undergoes x-ray induced decomposition, the photons damage the crystal lattice through absorption and decreases the peak intensity (Garman & Weik, 2023). Furthermore, this damage displaces the atoms and leads to an expansion or increase in the d-spacing of the crystal structure.

Global radiation damage

Decreased reflection intensities



Unit cell expansion

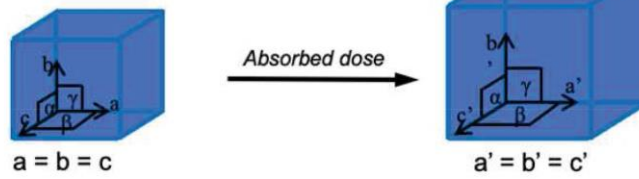


Figure 10: Radiation damage is characterized by decreased reflection intensities and unit cell expansion.

CHAPTER 4: EXPERIMENT

4.1: Sample Preparation

A mortar and pestle were used to grind the powders together during preparation [Fig. 11].

The grinding allows for the powder to be broken down into even smaller grains and promotes the random orientation needed for powder diffraction. This results in sharper images and peaks, enabling more precise measurements. An equation was derived to ensure the mixture had the correct ratios for the uracil and the element [Eqs. 17.1 and 17.2]. For the 90% uracil powder and 10% element powder mixture by mass:

$$\frac{M_{uracil}}{M_{uracil} + M_{element}} = 0.90 \quad \text{[Equation 17.1]}$$

$$M_{uracil} = 9M_{element} \quad \text{[Equation 17.2]}$$

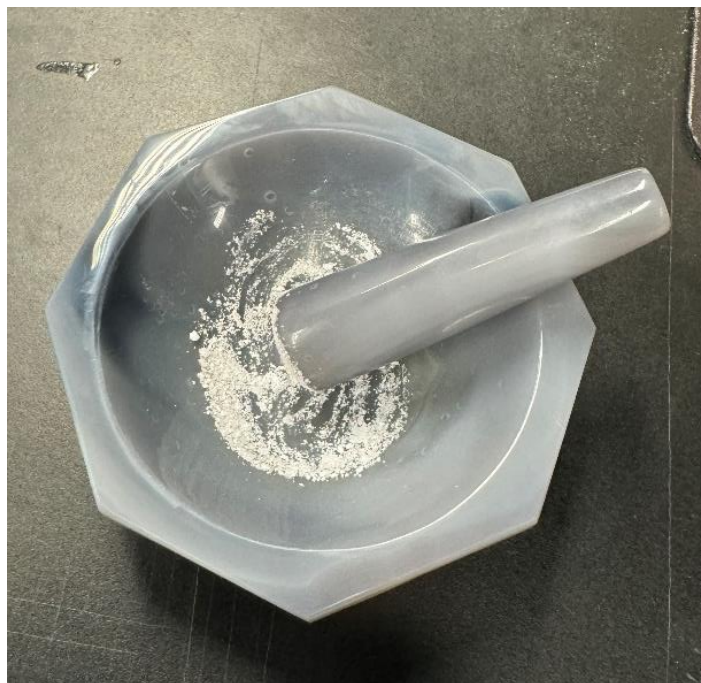


Figure 11: Mortar and pestle used for grinding.

After the powder was grinded it was placed into a quartz glass capillary tube with a length of 75mm and an inner diameter of 1.1 – 1.2 mm [Fig. 12].

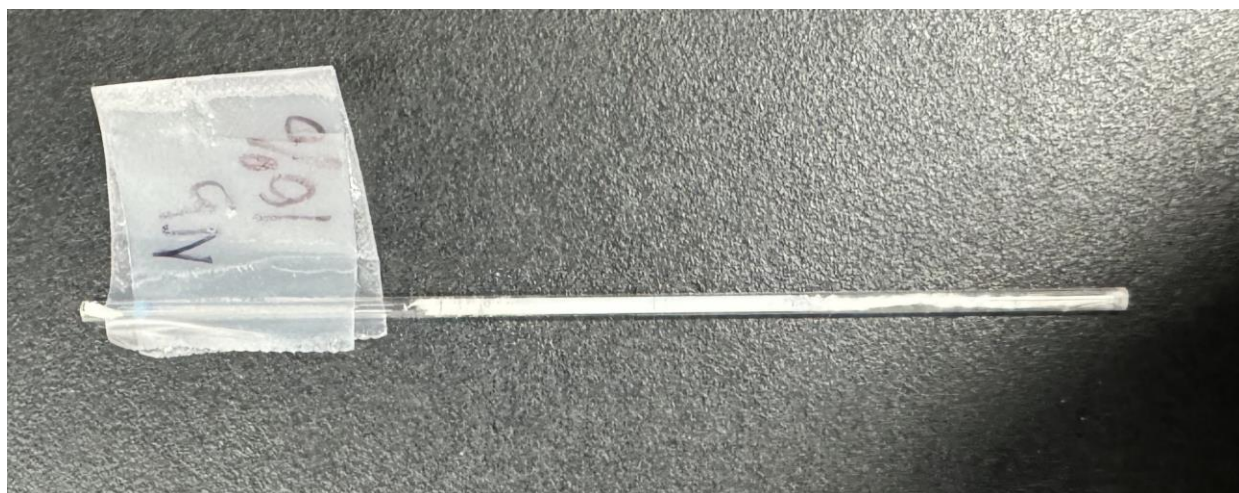


Figure 12: Capillary tube with a 90% Uracil + 10% Niobium sample.

It was important to eliminate the possibility that the decomposition was the result of heat generated by the x-ray beam rather than radiation. To confirm the decomposition was solely induced by the x-ray beam, a diamond anvil cell was utilized. This device leverages the hardness of diamonds to subject materials to extreme pressures (Katrusiak & McMillan, 2004). Diamonds have very high thermal conductivity that transfers heat efficiently and away from the sample. The specially designed diamond anvils have flat culets and are glued opposite to one another on seats made from hard materials like tungsten carbide.

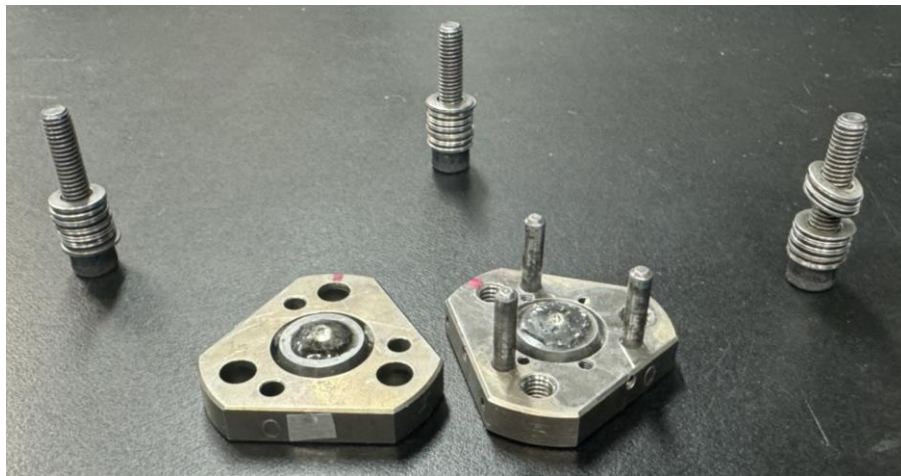


Figure 13: Disassembled diamond anvil cell.

The sample is placed in a gasket between the culets and the cell is closed. The socket head screws, used to tighten the cell, have Belleville washers that function as springs when force is generated. Tightening the screws increases the pressure on the sample by squeezing the diamond together. With openings on each side of the cell, the transparent nature of diamonds allows for a variety of optics and x-ray experiments [Fig. 13]. The pressure induced on the

sample is a ratio of the force generated by tightening the screws to the culet flat area [Eq. 18] (Ferraro, 2012).

$$P = \frac{F}{A} \quad \text{[Equation 18]}$$

A small amount of powder was placed to cover the culet and the DAC was gently closed. To hold the DAC together, the screws were slightly tightened to ensure the sample did not leak out [Fig. 15]. Lastly, the cell was examined under the microscope to ensure the sample remained between the culets [Fig. 14].

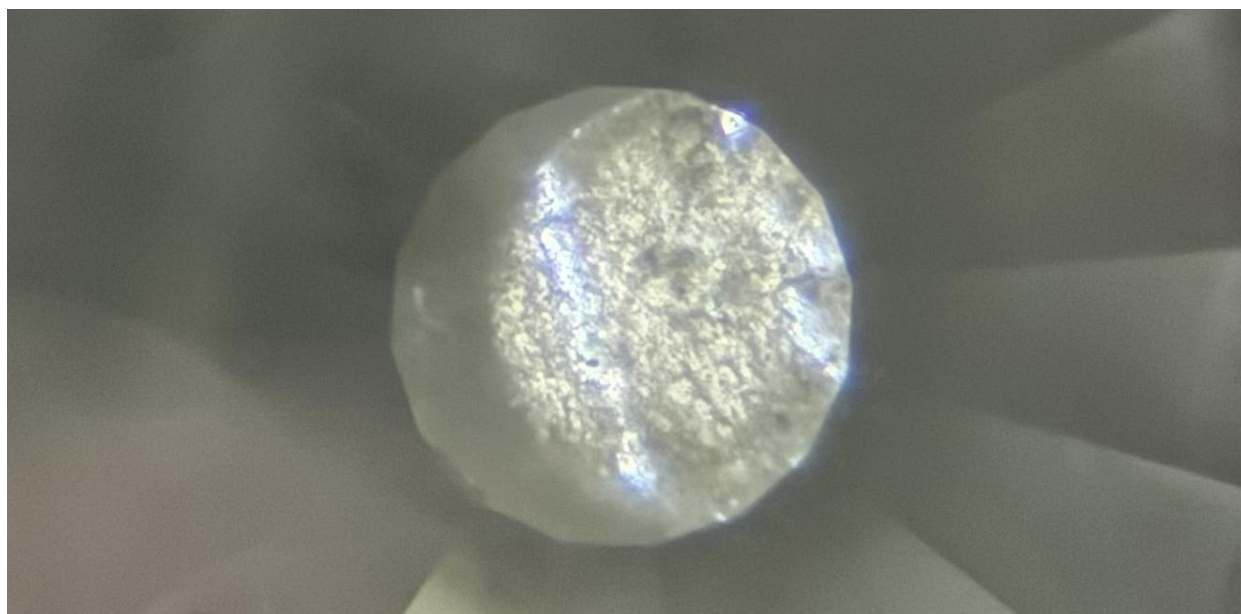


Figure 14: View of the culet in the closed cell with a microscope with the sample powder (90% Uracil + 10% Selenium) covering most of the culet.



Figure 15: Assembled diamond anvil cell.

4.2: Data Processing

The decomposition amount is represented as the decomposition yield $DY(t)$ with peak area after irradiation time $Area_t$ and initial peak area $Area_0$ [Eq. 19] (Goldberger et al., 2017):

$$DY(t) = \left(1 - \frac{Area_t}{Area_0}\right) \quad \text{[Equation 19]}$$

To characterize the transformation of the sample, a modified version of Avrami model was utilized [Eq. 20]. The Avrami equation was originally formulated to represent the kinetics of phase transformations in solids at a consistent temperature (Cantor, 2020). However, this formula

was later modified to analyze the crystalline growth due by making both the overall rate constant k and time t a function of the Avrami exponent n which characterizes the type of growth that occurs (Lua Sanchez et al., 2023). An Avrami exponent of less than or equal to one refers to one dimensional or linear growth (Evlyukhin et al., 2015). The decomposition yield at the end of the process DY_{∞} was set to 0.5 to ensure that the fit would converge successfully for each set of data.

$$DY(t) = DY_{\infty}(1 - e^{-(kt)^n}) \quad [\text{Equation 20}]$$

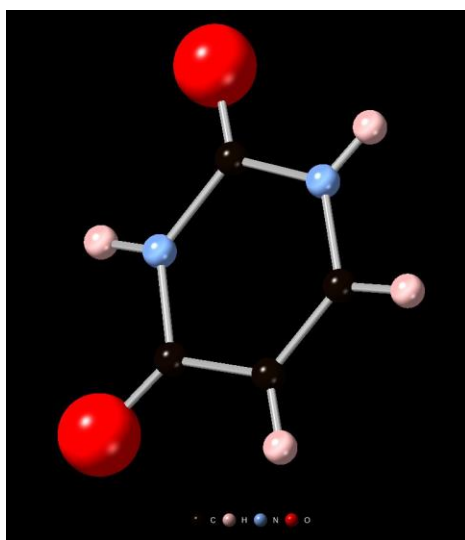


Figure 16: Uracil molecule from CrystalMaker software.

Monoclinic	a = 11.938 Å b = 12.376 Å c = 3.655 Å	$\alpha = \gamma = 90^\circ$ $\beta = 120.9^\circ$	Primitive
Volume = 463.386 Å ³			
Density = 1.607 g/cm ³			
Z = 8			

Table 2: Uracil parameters including crystal structure, axial lengths, axial angles, and Bravais lattice (Stewart & Jensen, 1967).

Uracil has a Monoclinic crystal structure and chemical formula of $C_4H_4N_2O_2$ (Fig. 16). To remain consistent throughout the entire experiment, the Uracil peak with the highest intensity was chosen for analysis. Furthermore, having the highest intensity allowed for the peak to be more easily seen in the presence of the doping elements. The peak with the highest intensity on the Uracil diffraction pattern had miller indices of (0 0 1) (Fig. 17).

Once the diffraction image was imported into Dioptas®, the background was subtracted and the 2θ range was limited to include the peak with the highest intensity (0 0 1). To determine the 2θ value at the peak's maximum intensity, the x-ray diffraction plot was imported into Origin to utilize the "Peak Analyzer" tool. The software uses a "Local Maximum Method" to determine the peak position. Origin analyzes every point on the curve to see if it is the extrema, a minimum or maximum among the entire range. Once a potential extremum is found, origin filters out the points that are 20% less than this value to ensure the value is the peak maximum. After the peak is determined, origin integrates the peak to determine the area. To fit the modified Avrami equation, Origin takes advantage of the Levenberg-Marquardt iteration method. After estimating an initial curve fit, the iteration method introduces a dampening factor λ . This factor controls the step size with a high λ translating to smaller steps for fitting until convergence is met.

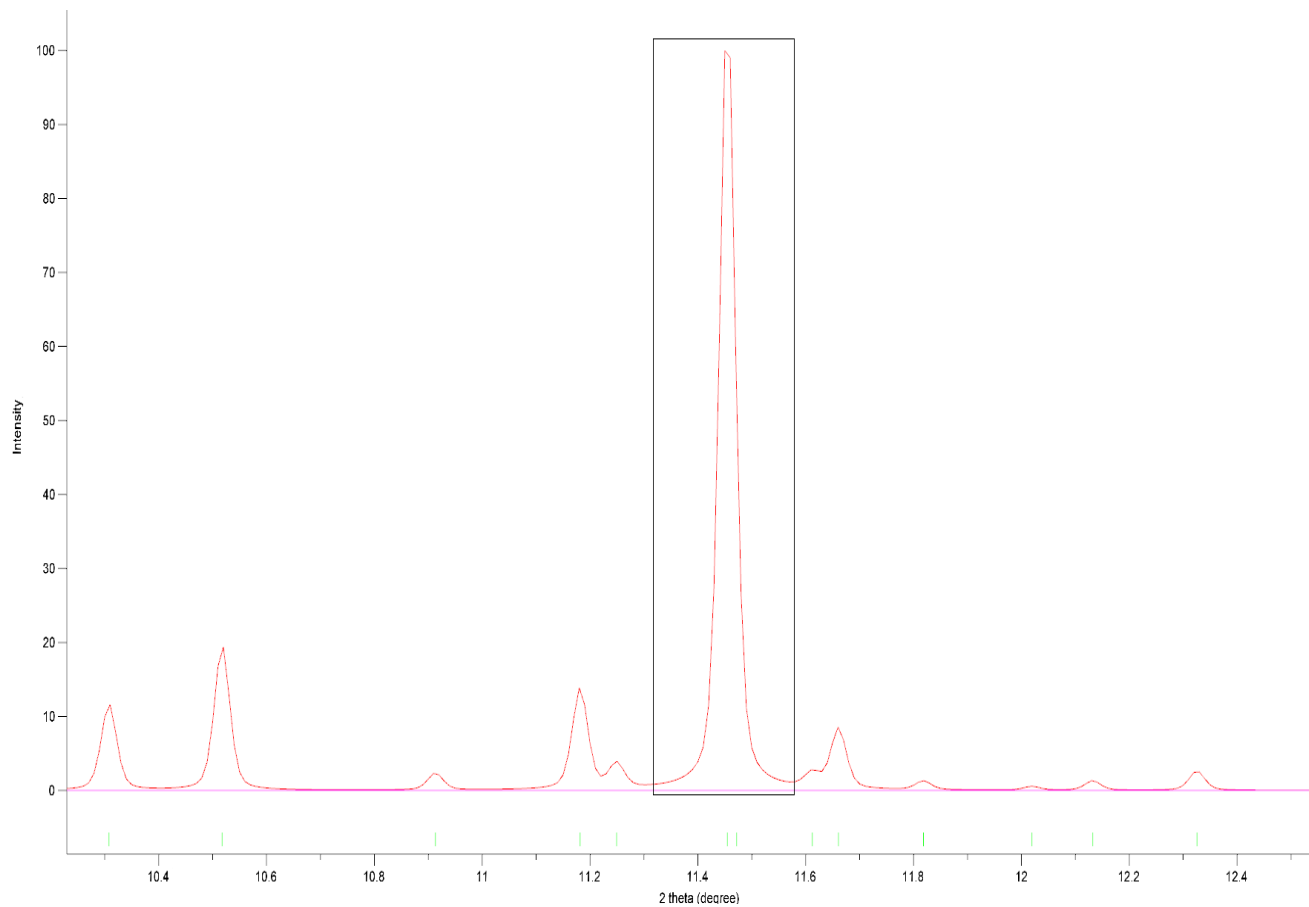


Figure 17: Uracil XRD plot at 19.8 keV. The boxed peak has miller indices of (0 0 1) and was chosen for data analysis from every XRD image.

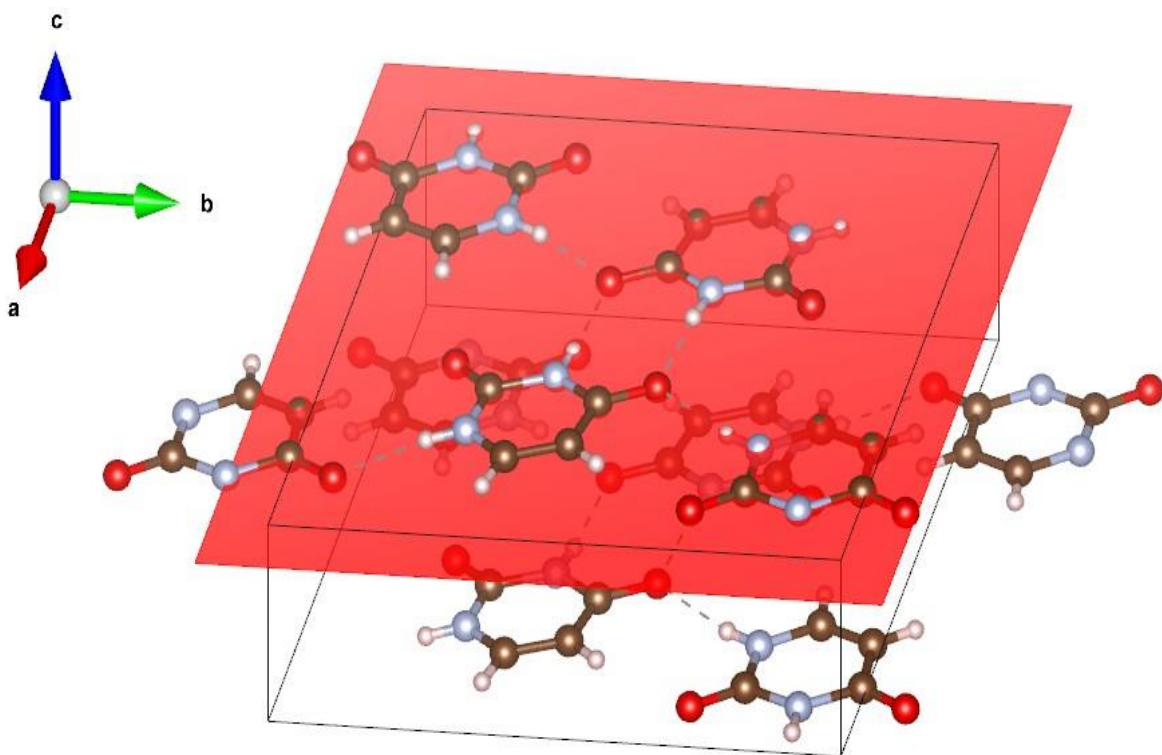


Figure 18: Uracil unit cell from VESTA. The lattice plane of miller indices (0 0 1) is highlighted in red.

CHAPTER 5: RESULTS and DISCUSSION

5.1: Gold

As gold has an L-I absorption edge at 14.3528 keV, a set of trials was conducted at 14.5 keV with two different samples: 100% Uracil and 90% Uracil + 10% Gold powder (Ethan Merritt, 2010). Lastly, the energy was raised by 1 keV to 15.7 keV and another 90% Uracil + 10% Gold sample was irradiated. All samples were irradiated for two hours.

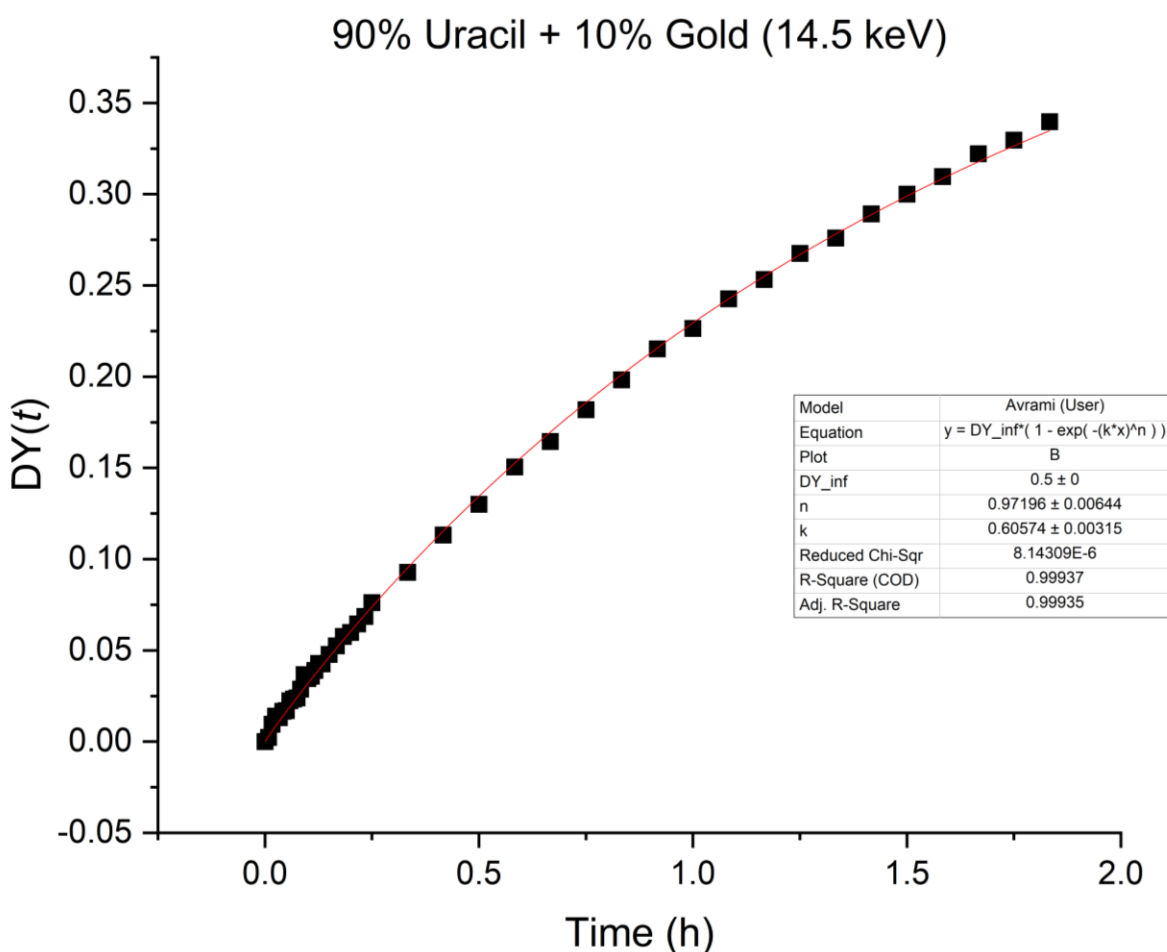


Figure 19: Plot and fit of doped uracil sample at 14.5 keV with modified Avrami equation fit results.

90% Uracil + 10% Gold (14.5 keV)	
DY_{∞}	0.5
n	0.97196 ± 0.00644
k (h ⁻¹)	0.60574 ± 0.00315

Table 3: Modified Avrami fit parameters from (Fig. 19).

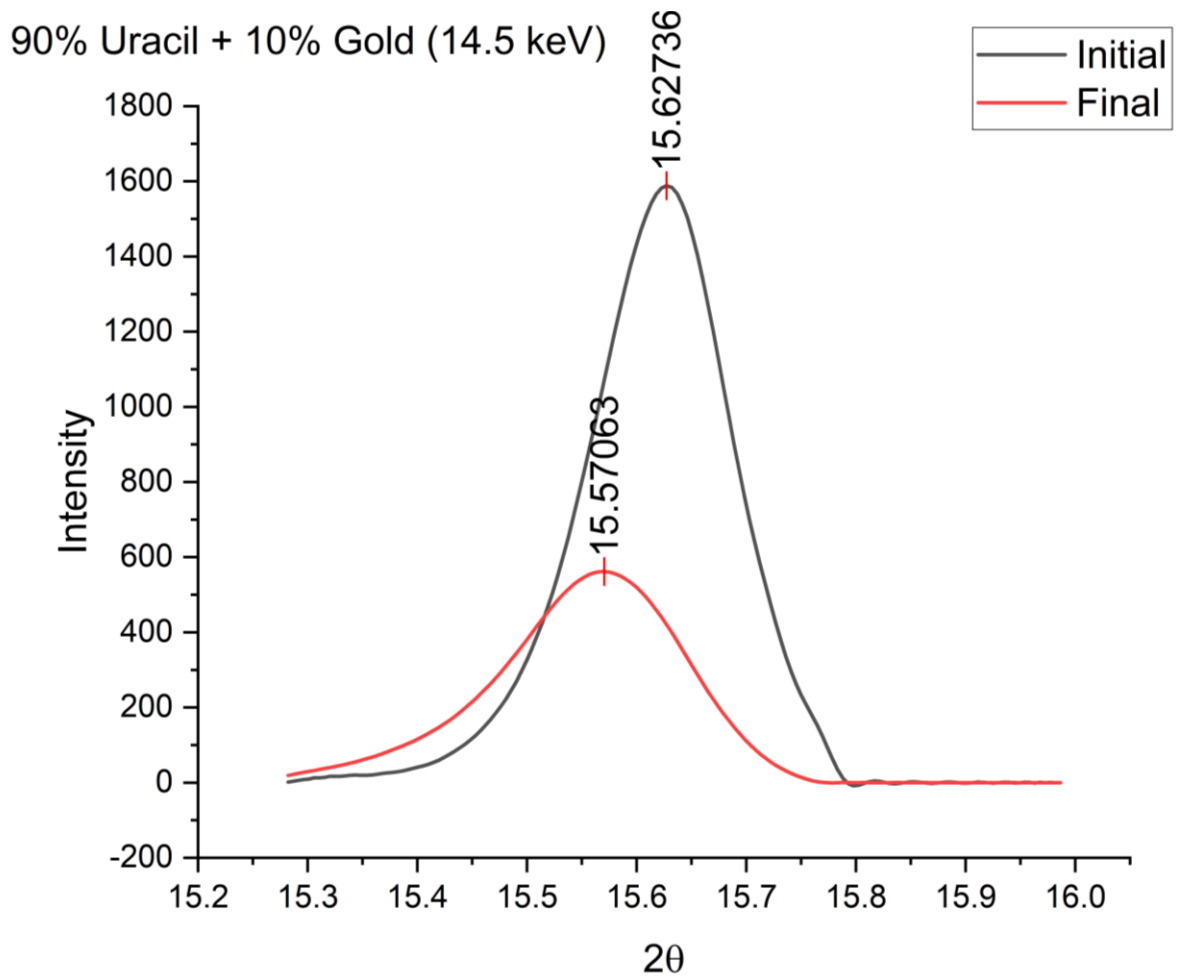


Figure 20: Initial and final uracil peak overlaid from the doped sample at 14.5 keV.

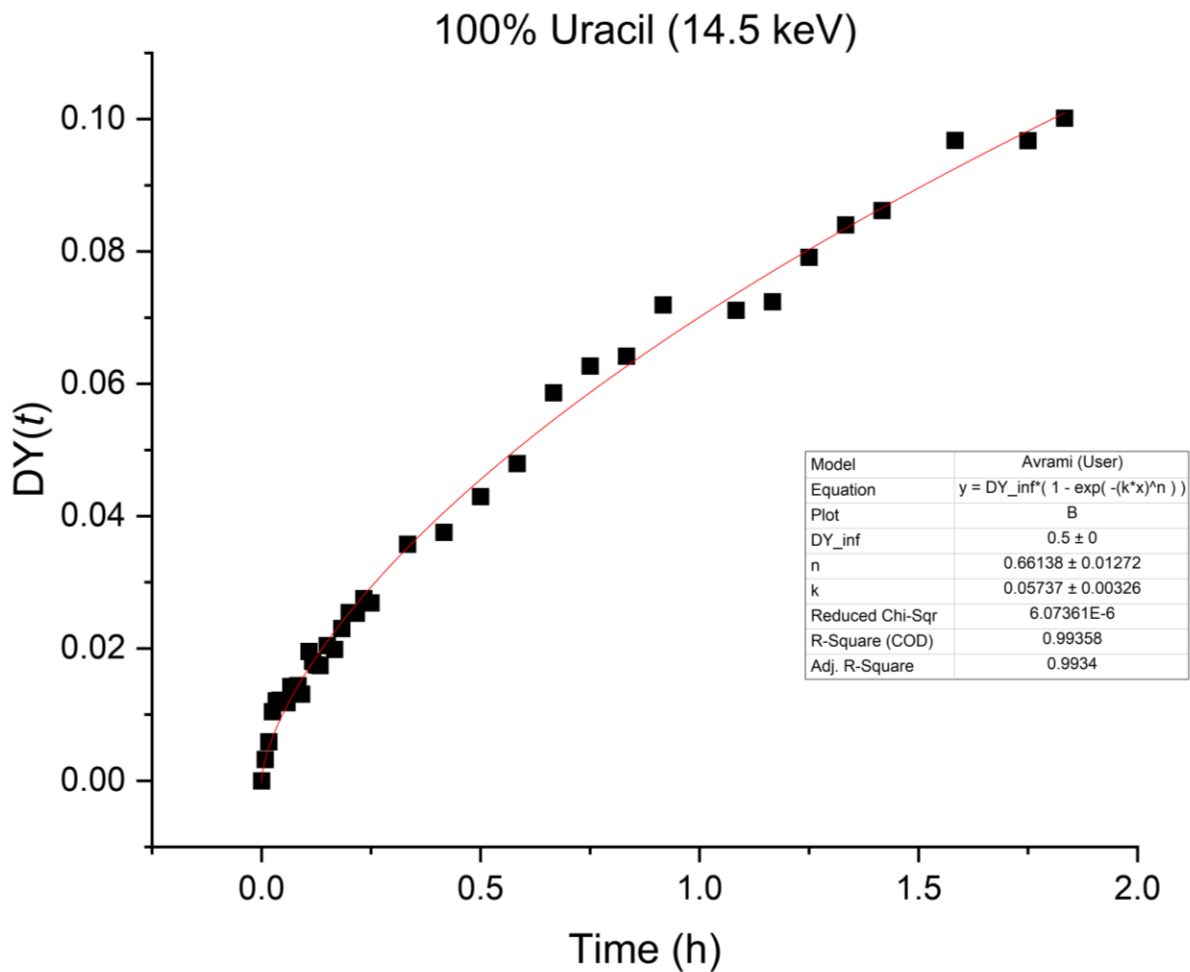


Figure 21: Plot and fit of a pure uracil sample at 14.5 keV with the modified Avrami equation results.

100% Uracil (14.5 keV)	
DY _∞	0.5
n	0.66138 ± 0.01272
k (h ⁻¹)	0.05737 ± 0.00326

Table 4: Modified Avrami fit parameters from (Fig. 21).

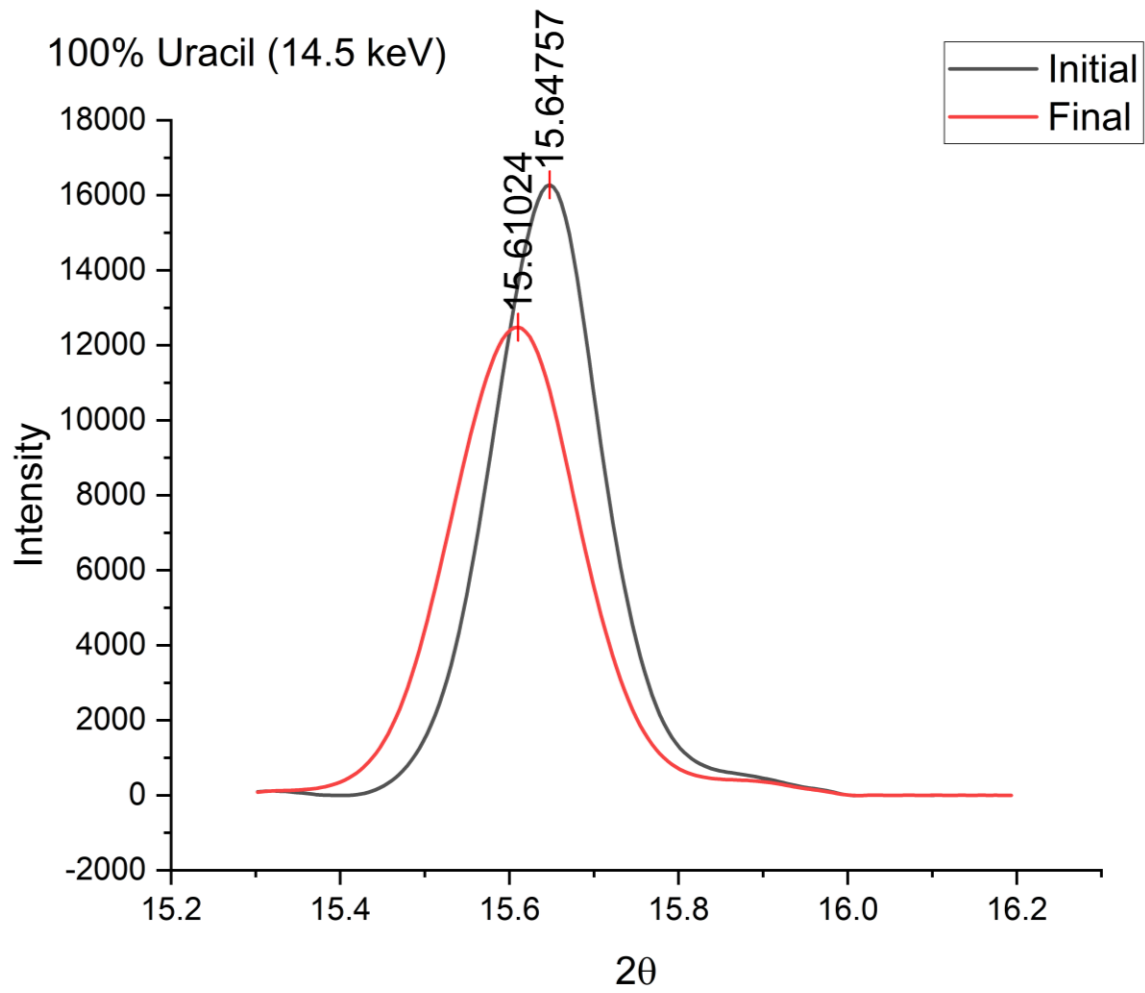


Figure 22: Initial and final uracil peak overlaid from the virgin uracil sample at 14.5 keV.

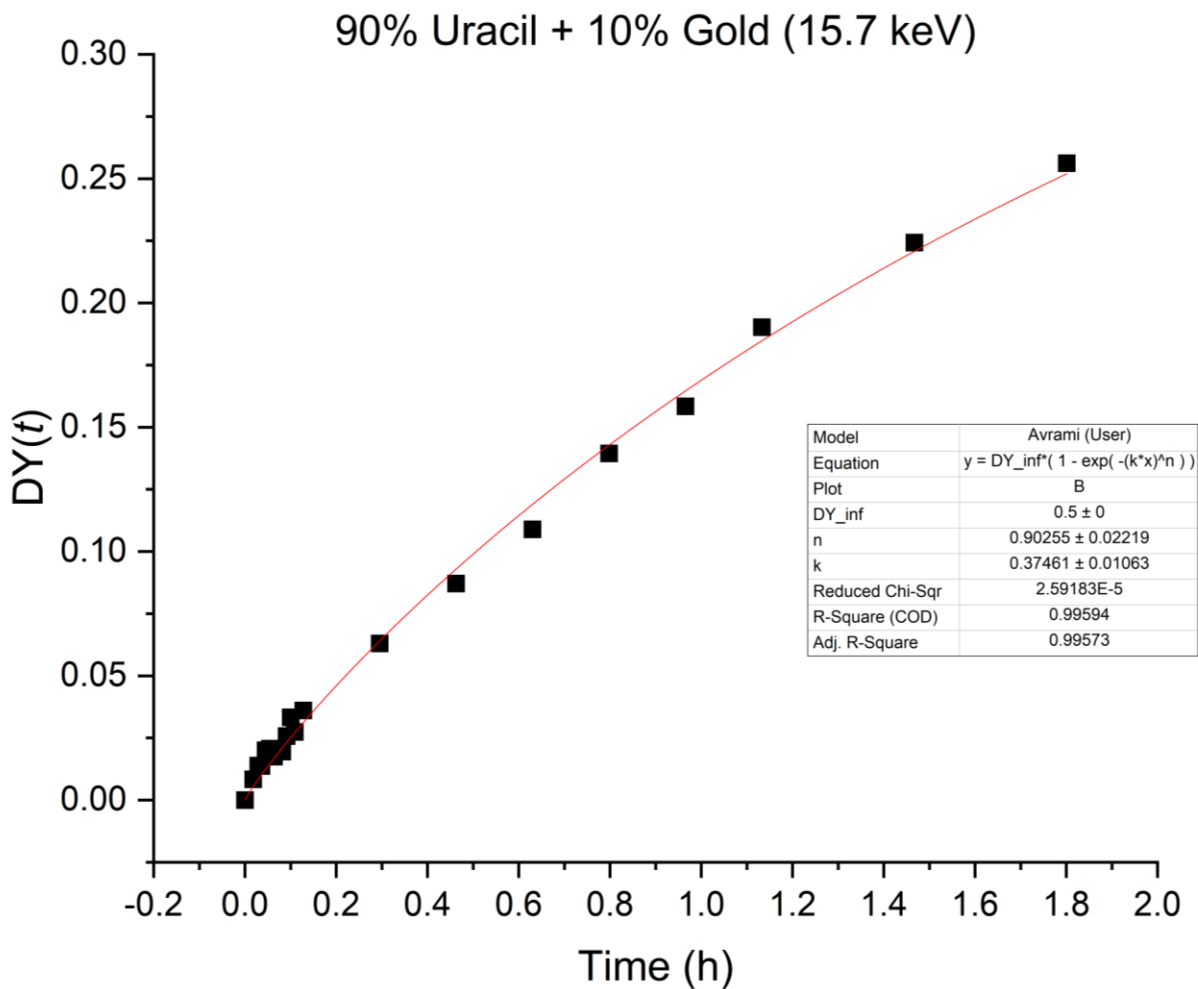


Figure 23: Plot and fit of a doped uracil sample at 15.7 keV with the modified Avrami equation results.

90% Uracil + 10% Gold (15.7 keV)	
DY_{∞}	0.5
n	0.90255 ± 0.02219
k (h^{-1})	0.37461 ± 0.01063

Table 5: Modified Avrami fit parameters from (Fig. 23).

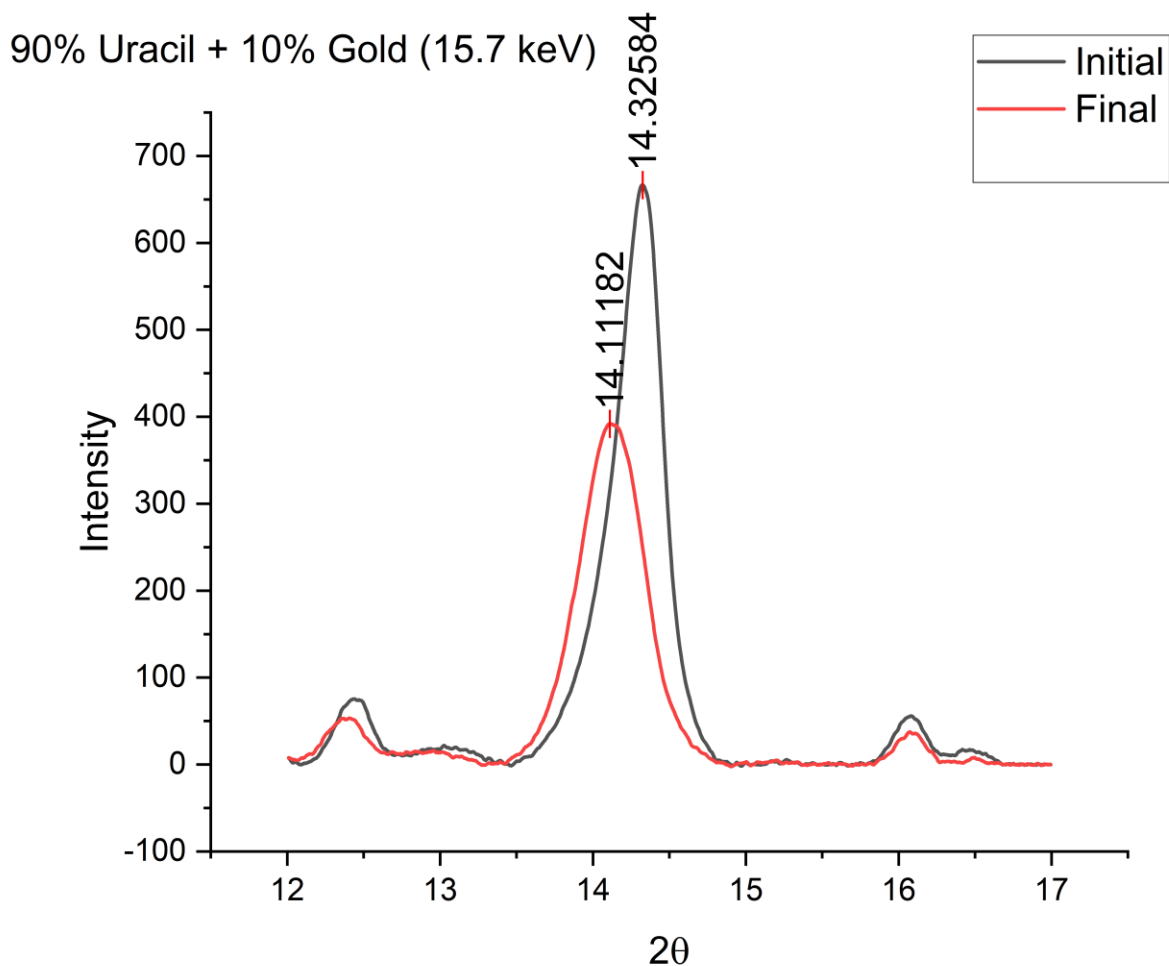


Figure 24: Initial and final uracil peak overlaid from the doped uracil sample at 15.7 keV.

5.2: Selenium

With the k-edge of Selenium at 12.6578 keV, new samples were irradiated at an energy of 12.721 keV (Ethan Merritt, 2010). Two DAC trials were conducted for just under two and a half hours: 90% Uracil + 10% Selenium and 100% Uracil. The goal of utilizing a diamond anvil cell (DAC) was to confirm that the radiation damage from the exposure to the x-ray beam induced the decomposition.

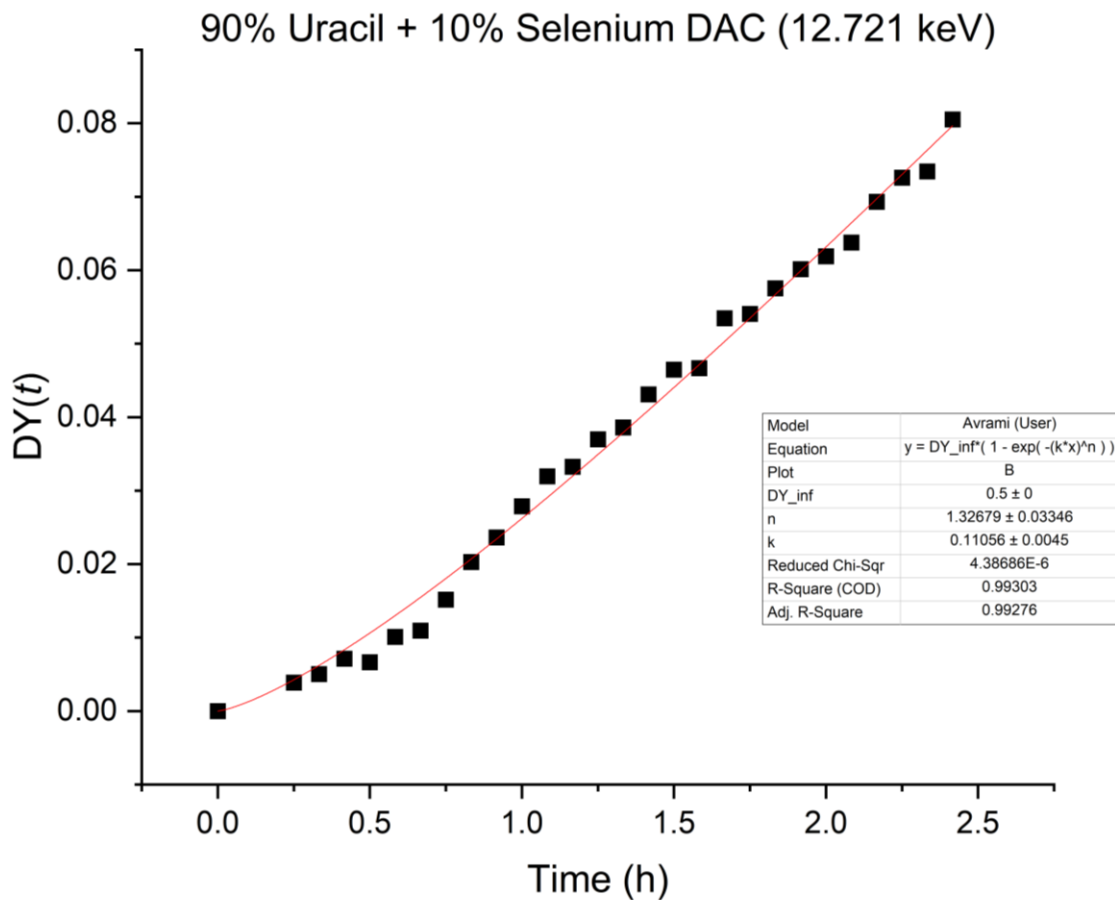


Figure 25: Plot and fit of a doped uracil sample in the DAC at 12.721 keV with the modified Avrami equation results.

90% Uracil + 10% Selenium DAC (12.721 keV)	
DY_{∞}	0.5
n	1.32679 ± 0.03346
k (h^{-1})	0.11056 ± 0.0045

Table 6: Modified Avrami fit parameters from (Fig. 25).

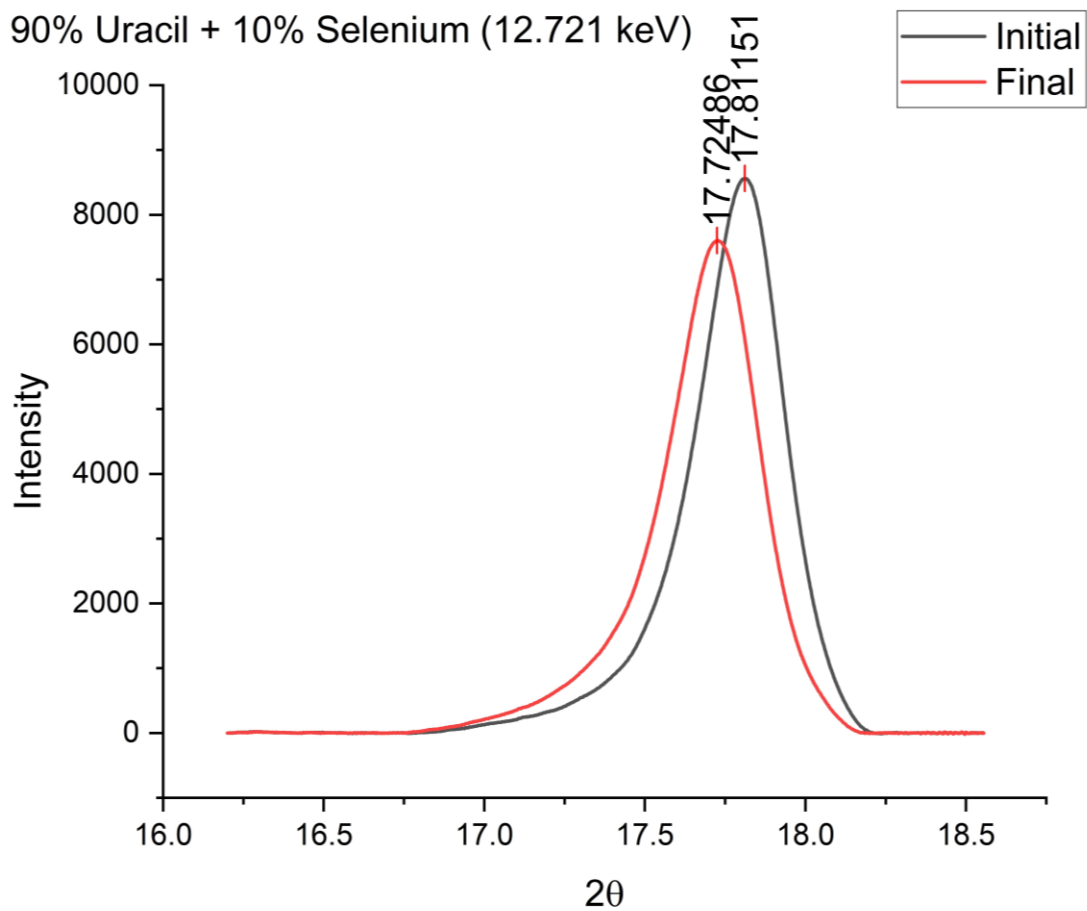


Figure 26: Initial and final uracil peak overlayed from the doped uracil sample in the DAC at 12.721 keV.

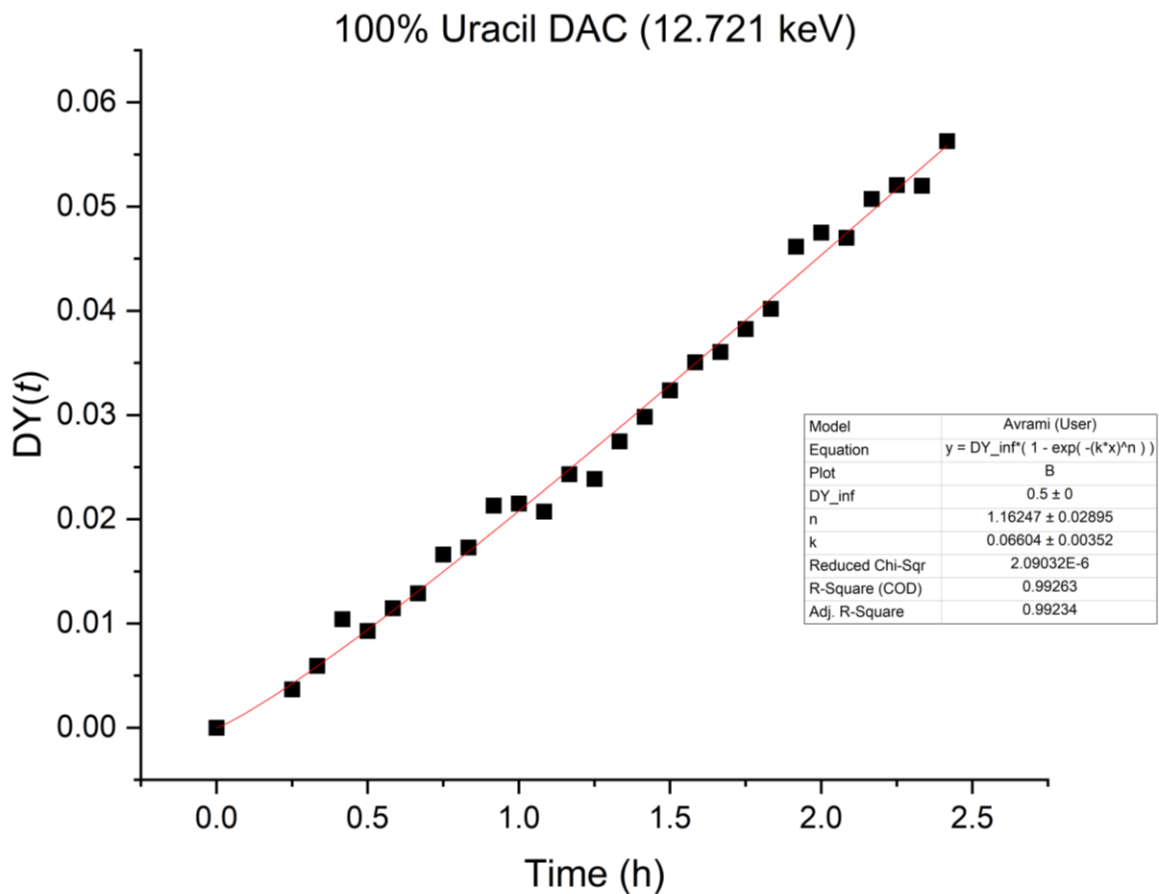


Figure 27: Plot and fit of a pure uracil sample in the DAC at 12.721 keV with the modified Avrami equation results.

100% Uracil DAC (12.721 keV)	
DY_{∞}	0.5
n	1.16247 ± 0.02895
k (h ⁻¹)	0.06604 ± 0.00352

Table 7: Modified Avrami fit parameters from (Fig. 27).

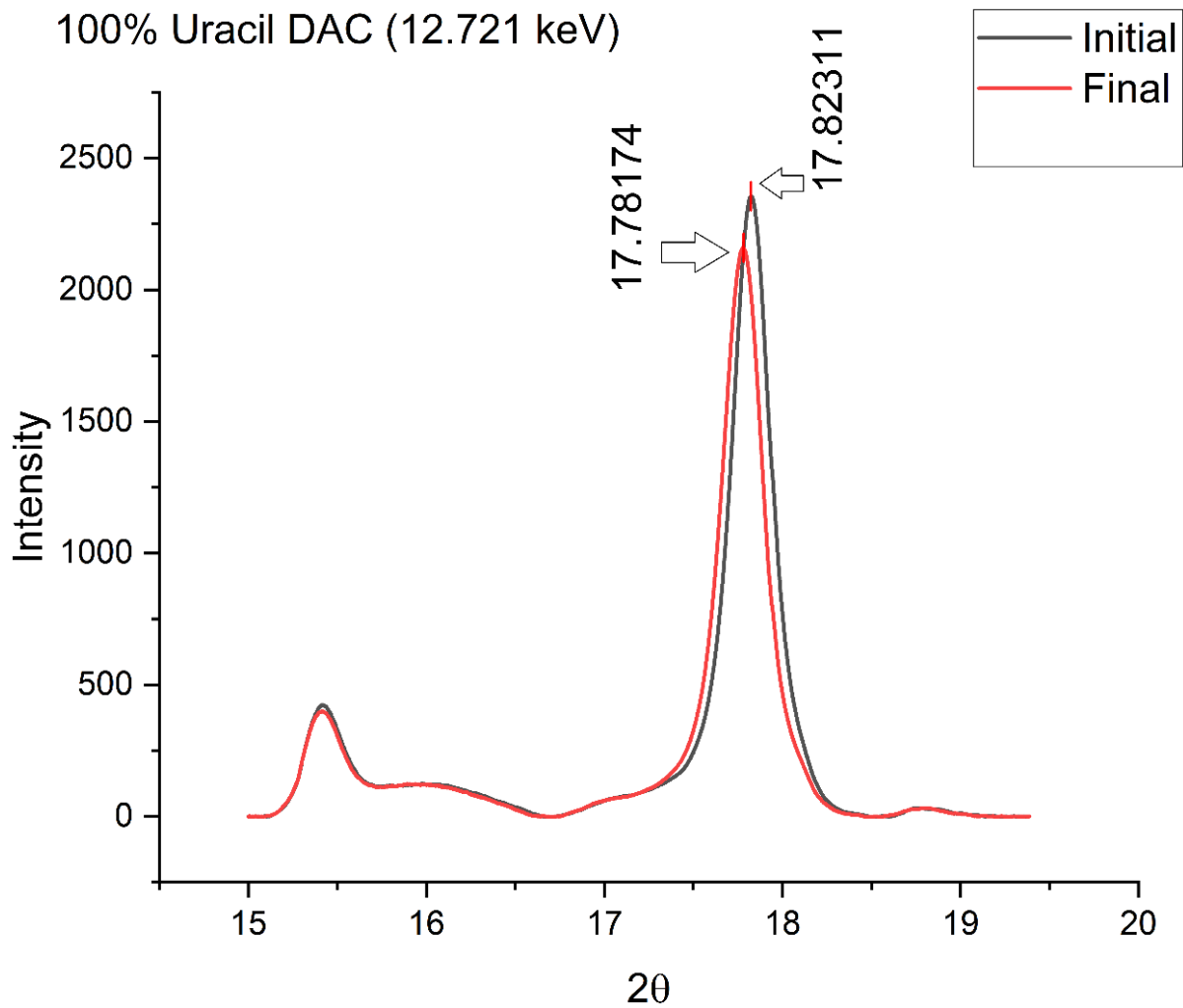


Figure 28: Initial and final uracil peak overlayed from the pure uracil sample in the DAC at 12.721 keV.

5.3: Niobium

Two different niobium samples were tested during the experiment: 100% uracil and 90% uracil + 10% niobium samples. As the K-edge of Niobium is 18.9856 keV, the virgin sample and the doped sample were irradiated at 19.581 keV for a little over four hours each (Ethan Merritt, 2010).

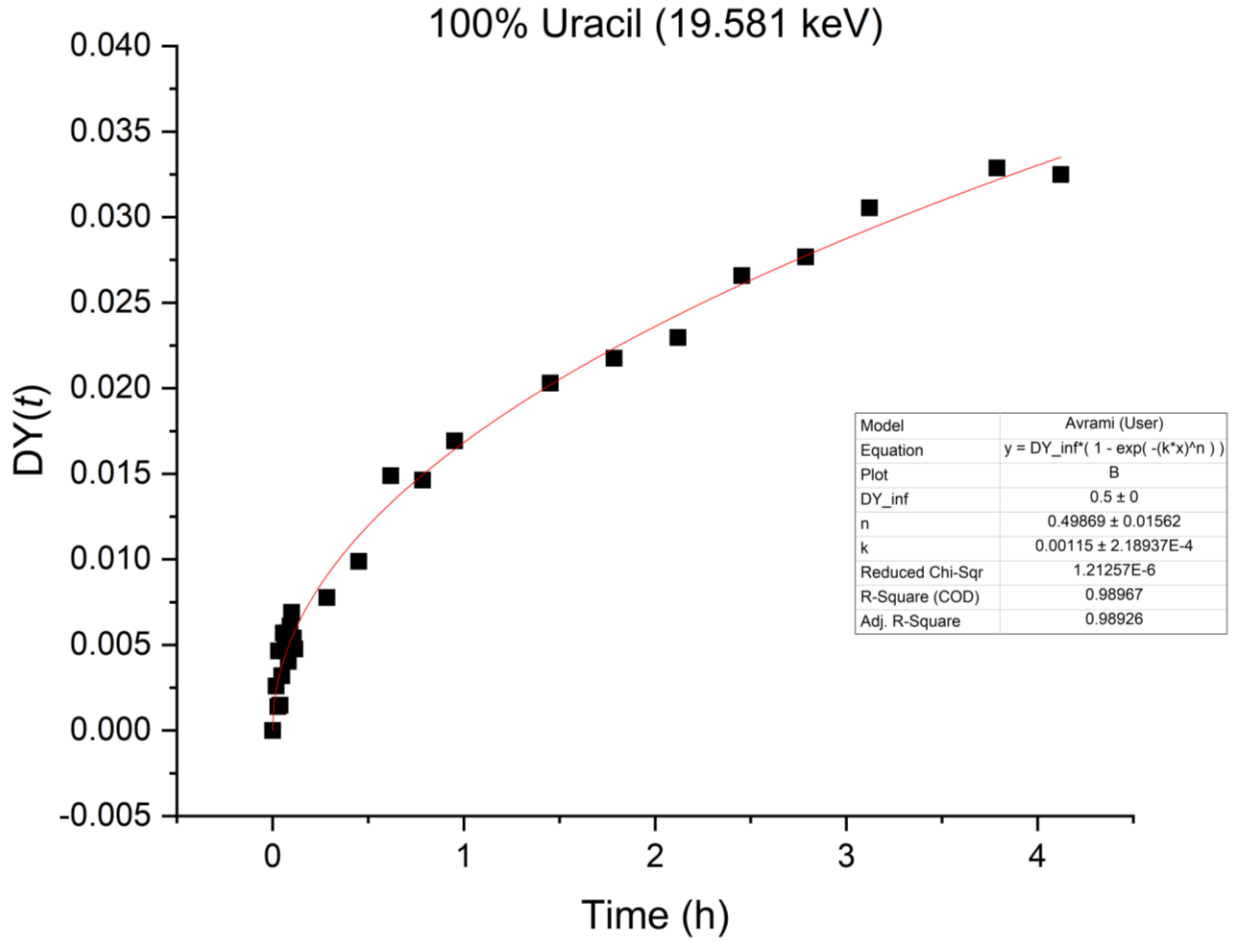


Figure 29: Plot and fit of a pure uracil sample in the at 19.581 keV with the modified Avrami equation results.

100% Uracil (19.581 keV)	
DY _∞	0.5
n	0.49869 ± 0.01562
k (h ⁻¹)	$0.00115 \pm 2.18937E-4$

Table 8: Modified Avrami fit parameters from (Fig. 29).

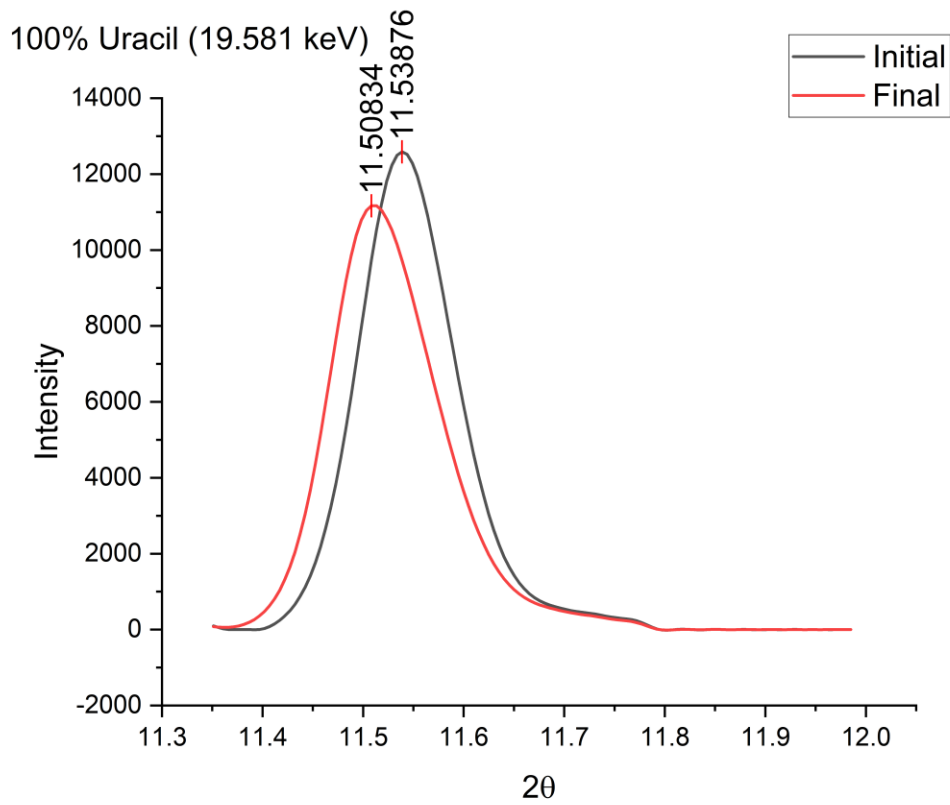


Figure 30: Initial and final uracil peak overlayed from the pure uracil sample at 19.581 keV.

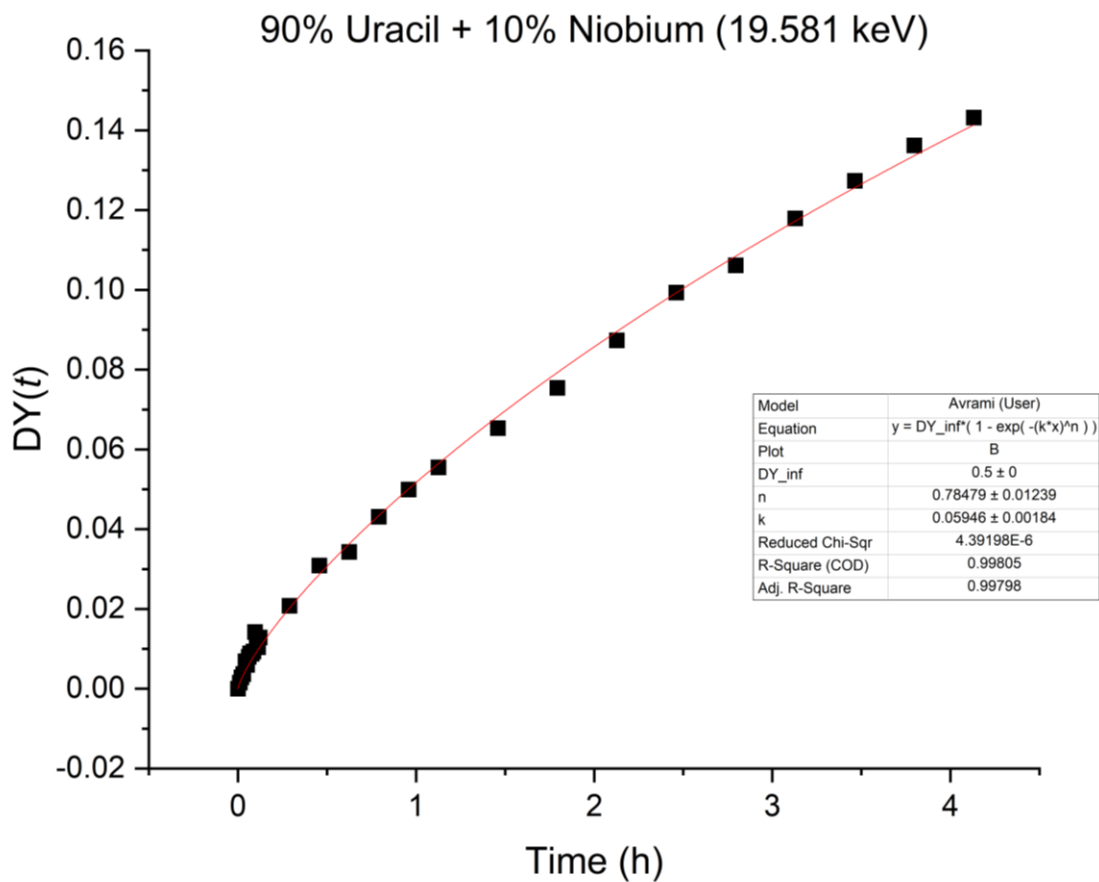


Figure 31: Plot and fit of the doped uracil sample in the at 19.581 keV with the modified Avrami equation results.

90% Uracil + 10% Niobium (19.581 keV)	
DY_∞	0.5
n	0.78479 ± 0.01239
k (h^{-1})	0.05946 ± 0.00184

Table 9: Modified Avrami fit parameters from (Fig. 31).

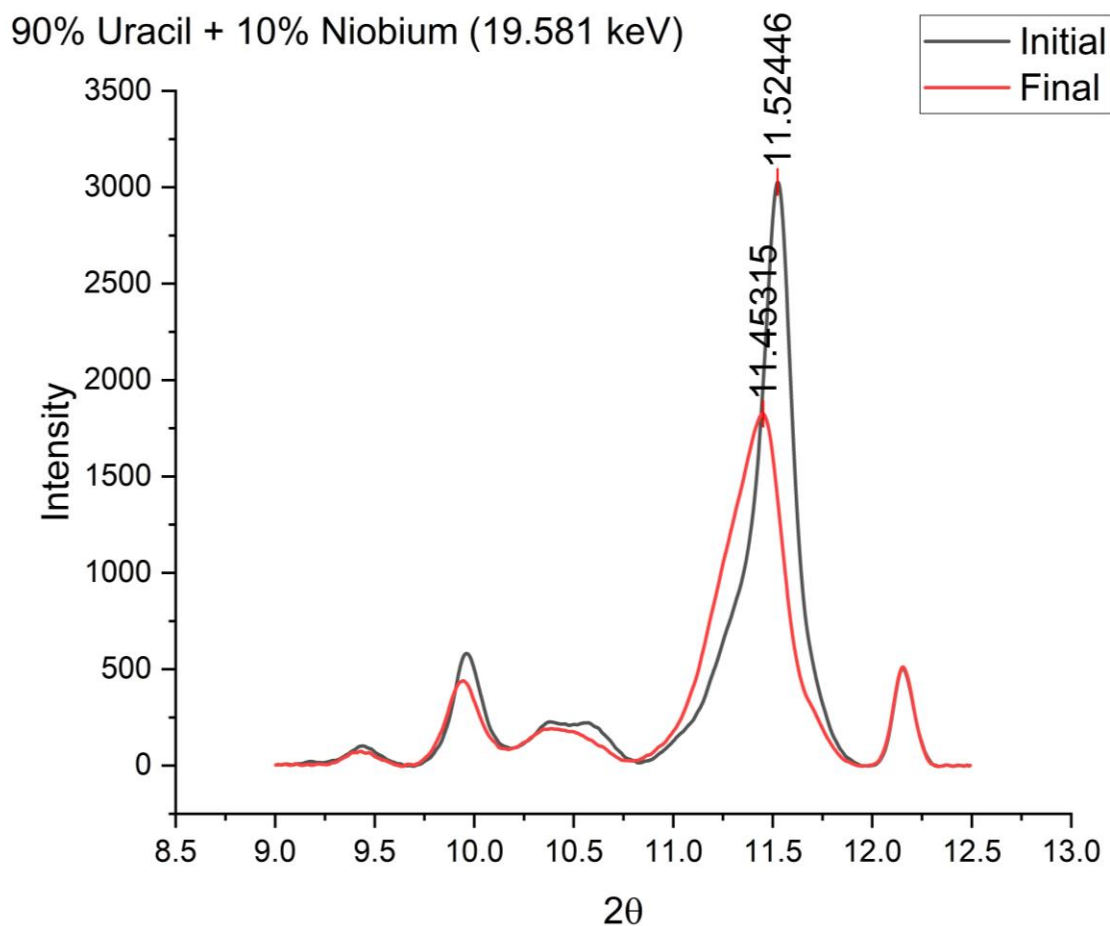


Figure 32: Initial and final uracil peak overlayed from the doped uracil sample at 19.581 keV.

5.4: Discussion

After isolating the uracil peak and overlaying the diffraction plots for each energy, the uracil peak decreased in intensity while simultaneously shifting to a lower 2θ (Figs. 20, 22, 24, 26, 28, 30, 32). According [Eq. 9.2], the d-spacing is inversely proportional to $\sin \theta$. Therefore, a decrease in the diffraction angle translates to an increase in the d-spacing. With an increase in d-spacing, the bonds decompose as the unit cell expands. This combined with a decrease in intensity are the two major signs of radiation damage, leading to decomposition. All figures either had an Avrami exponent less than or approximately one, leading to the conclusion that the

decomposition yield growth was linear. The doped samples had a higher overall rate constant than the virgin Uracil samples (Figs. 19, 21, 23, 25, 27, 29, 31).

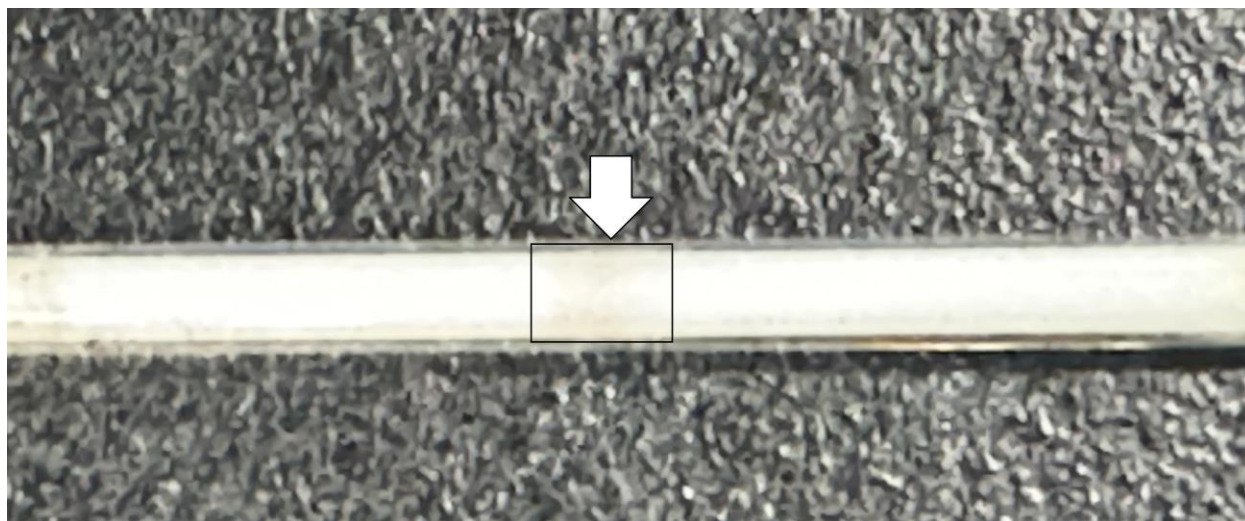


Figure 33: Damaged capillary tube. The damage caused slight discoloration.

The increase in decomposition is due to the photoelectric effect. As the x-ray photons are slightly above the electron binding energy, electrons eject from their respective shells. These photoelectrons begin to bombard the Uracil matrix with kinetic energy (Eq. 5) and provide enhanced decomposition. Furthermore, characteristic x-rays were emitted with their own energy from the element as the inner shell vacancy is filled by relaxation. The combination of the photoelectrons and characteristic x-rays enhance the radiation damage as they continue to strike the Uracil crystal structure.

However, despite having a higher energy, the decomposition rate at 15.7 keV is about 60% lower than at 14.5 keV, emphasizing the importance of absorption over energy level. In terms of quantum mechanics, absorption edges give the highest probability that an electron will

absorb the x-ray photon. Although both 14.5 keV and 15.7 keV are above the electron binding energy for the L-1 shell, 14.5 keV is much closer to the L-1 absorption edge (14.3528 keV). This creates a much higher probability of absorption and the subsequent photoelectric effect.

While the element to uracil ratios were identical for each doped sample, the 90% Uracil + 10% Gold decomposed significantly faster than the Niobium and Selenium doped samples. This is to be expected as Gold is a much heavier element with a higher atomic mass. With its high atomic number, the element also has significantly more electrons which introduced more shells and subshells. Therefore, gold can undergo a much wider range of electron transitions to fill the vacancy following the ejection of an L-1 shell electron. As a result, Gold has the probability to emit many more characteristic x-rays than Niobium or Selenium which resulted in enhanced decomposition. Furthermore, Gold has a significantly higher density than Selenium and Niobium. Having a higher density leads to more atoms packed in a specific area or a greater cross-sectional area for absorption. This tighter packing translates to a greater probability of the x-ray photons being absorbed by the electrons to induce the photoelectric effect (van Bokhoven & Lamberti, 2016).

CHAPTER 6: CONCLUSION

The experiment focused on enhancing the radiation damage of uracil, a nucleobase of RNA, and were conducted with x-ray diffraction at the Brockhouse House Undulator Beamline at the Canadian Light Source synchrotron in Saskatoon, Saskatchewan, Canada. Pure uracil samples were compared to samples doped 10% by mass with Gold, Niobium, and Selenium. In each x-ray diffraction plot, the uracil peak with the highest intensity (0 0 1) was isolated and integrated. After irradiation, the uracil peak experienced a decrease in intensity and an increase in the d spacing. These two results are the hallmark signs of x-ray induced radiation damage.

The calculated area was used to formulate a decomposition yield to plot as a function of time and fit with a modified Avrami equation. This fitting provided a rate constant k and an Avrami exponent n . The uracil in the doped samples decomposed faster than the virgin samples after irradiation, with Gold providing the highest rate constant. Furthermore, the Avrami exponent n quantified the decomposition behavior as being one-dimensional. To confirm the decomposition was due to x-ray irradiation and not heat, samples were tested in a diamond anvil cell (DAC) as the diamonds act as a heatsink and pull heat away from the sample. The DAC results displayed a decrease in intensity and an increase in d-spacing which confirmed that the decomposition of uracil was due to radiation damage.

The increased radiation damage is attributed to the photoelectric effect from irradiating the doped uracil with x-ray photons slightly above the dopant's absorption edge. Enhanced decomposition to the uracil crystal structure occurred from the release of photoelectrons and characteristic x-rays. These two byproducts of the photoelectric effect continuously bombard the uracil matrix and enhance the decomposition rate.

With more electrons, Gold is a strong absorber of x-rays photons leading to an increase in the probability of the photoelectric effect. Furthermore, Gold has a wider spectrum of characteristic x-rays. This combination led to a significantly higher rate constant k when compared to Niobium and Selenium. Moreover, increasing the x-ray photon energy did not lead to an increase in the decomposition as being further away from the absorption edge leads to a decrease in the probability of absorption. These results provide a new outlook on enhancing the radiation damage by the introduction of dopants to the sample.

APPENDIX

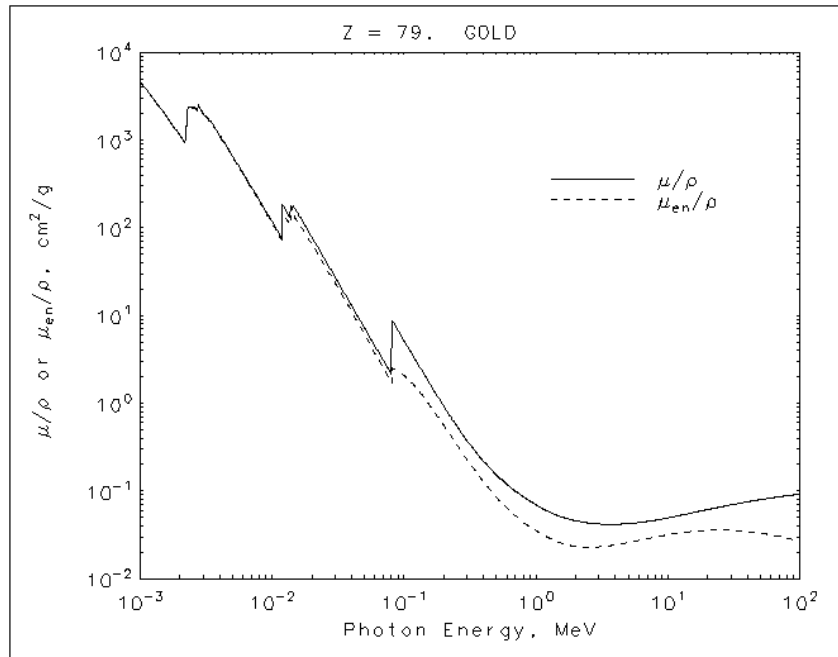


Figure 34: Mass energy-absorption coefficient for Gold as a function of the photon energy. The sharp increases in the coefficient represent the absorption edges (National Institute of Standards and Technology, 2004).

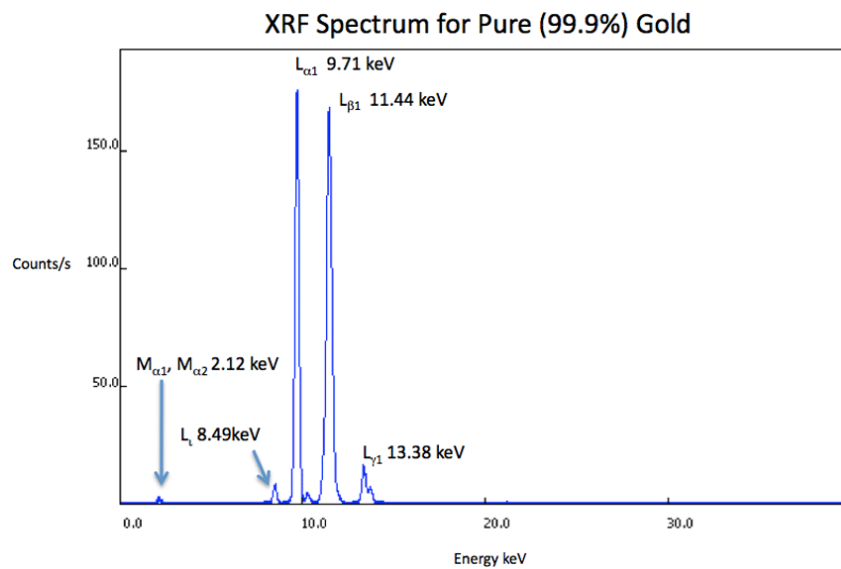


Figure 35: Spectrum of Gold's characteristic x-rays (XRF RESEARCH, 2024).

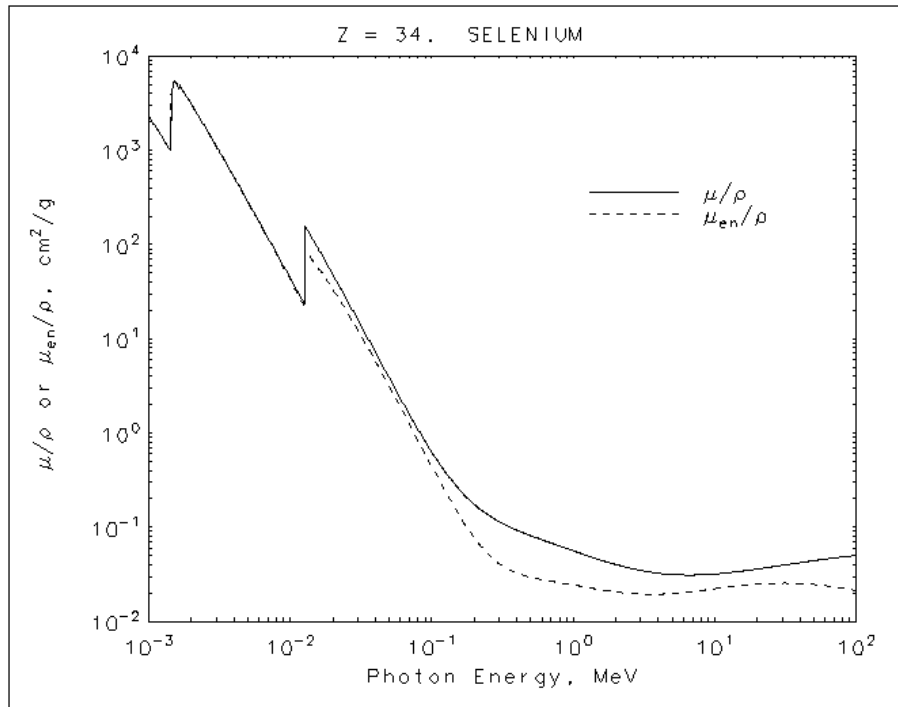


Figure 36: Mass energy-absorption coefficient for Selenium as a function of the photon energy. The sharp increases in the coefficient represent the absorption edges (National Institute of Standards and Technology, 2004).

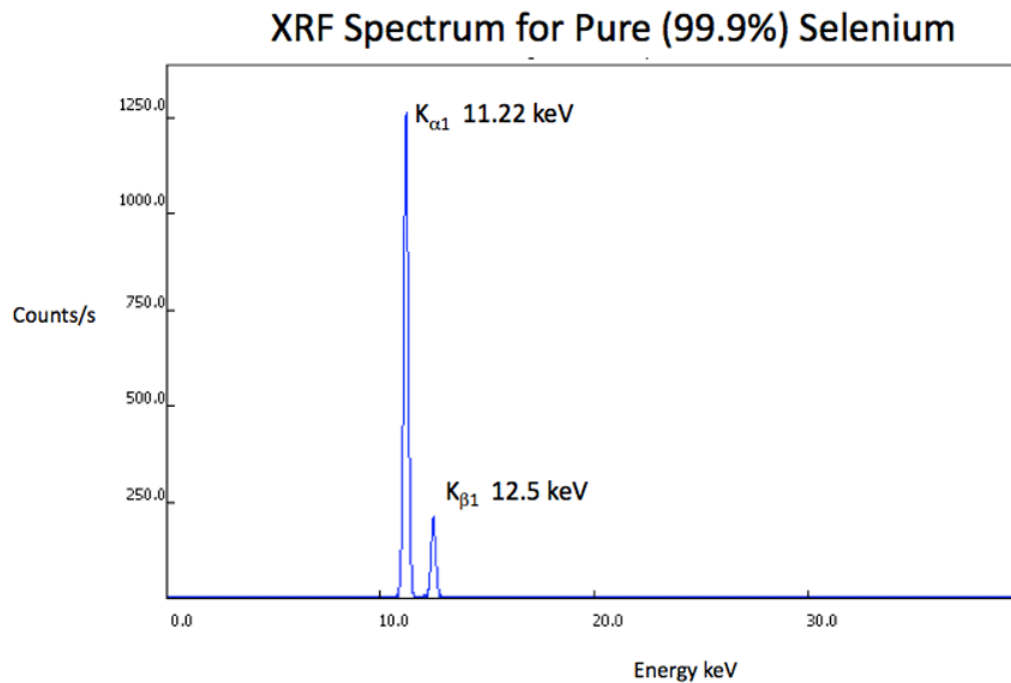


Figure 37: Spectrum of Selenium's characteristic x-rays (XRF RESEARCH, 2024).

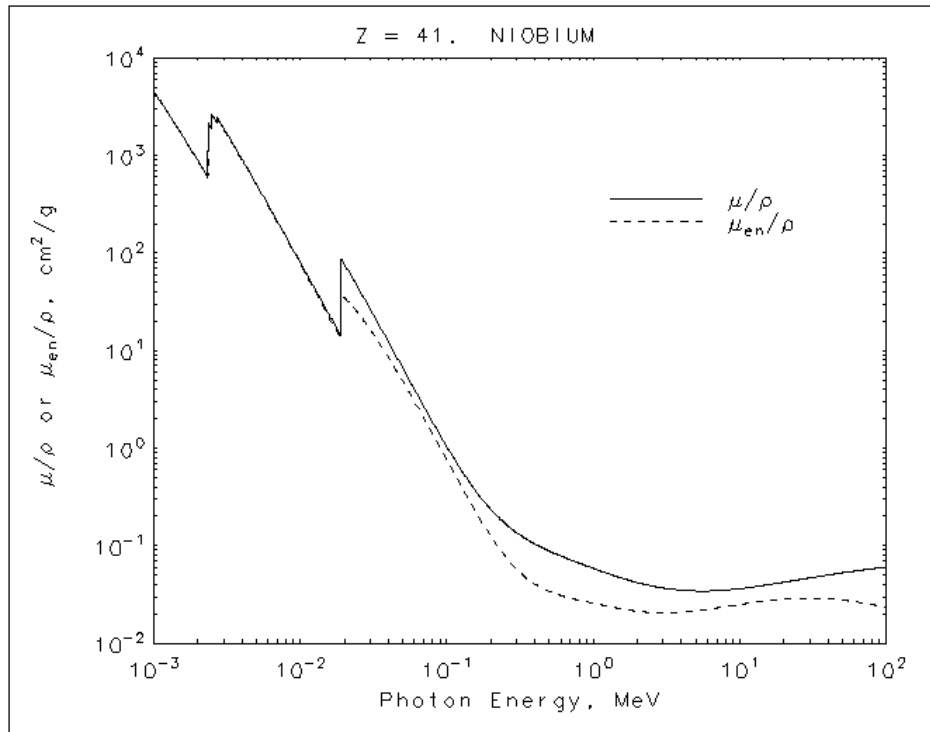


Figure 38: Mass energy-absorption coefficient for Niobium as a function of the photon energy. The sharp increases in the coefficient represent the absorption edges (National Institute of Standards and Technology, 2004).

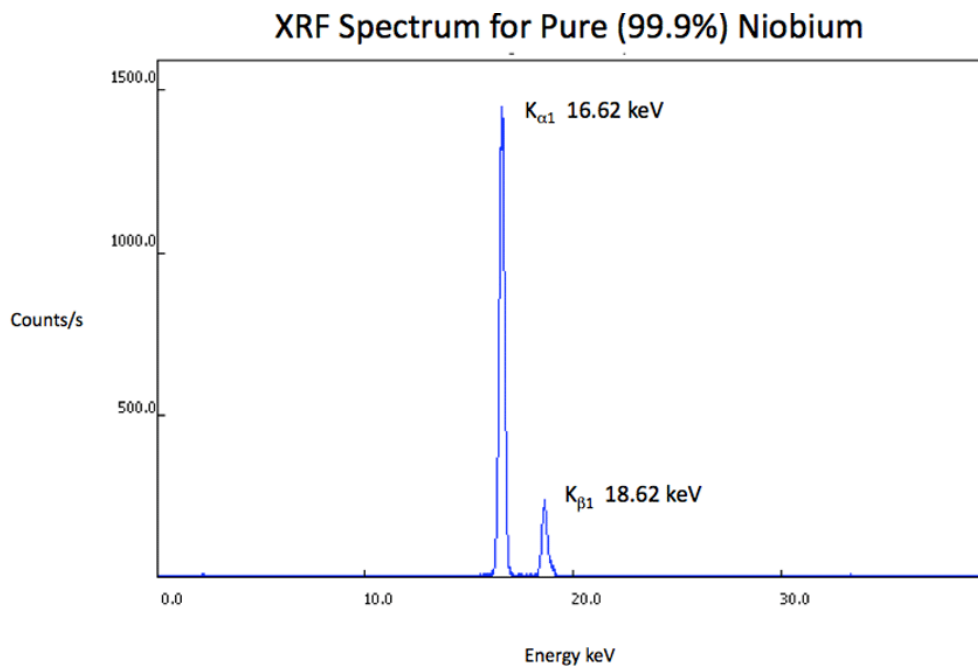


Figure 39: Spectrum of Niobium's characteristic x-rays (XRF RESEARCH, 2024).

WORKS CITED

- Bunker, G. (2010). *Introduction to XAFS: A Practical Guide to X-ray Absorption Fine Structure Spectroscopy*. Cambridge University Press.
<https://books.google.com/books?id=u6ggAwAAQBAJ>
- Canadian Light Source, & University of Saskatchewan. (n.d.-a). *BXDS - Brockhouse Diffraction Sector*.
- Canadian Light Source, & University of Saskatchewan. (n.d.-b). *What is a synchrotron?: Parts of the synchrotron*.
- Cantor, B. (2020). *The Equations of Materials*. Oxford University Press.
<https://doi.org/10.1093/oso/9780198851875.001.0001>
- Chattopadhyay, D. (2006). *Electronics (fundamentals And Applications)*. New Age International (P) Limited. https://books.google.com/books?id=n0rf9_2ckeYC
- Codling, K., Kunz, C., Gudat, W., Koch, E. E., Kotani, A., Lynch, D. W., Rowe, E. M., Sonntag, B. F., & Toyozawa, Y. (2013). *Synchrotron Radiation: Techniques and Applications*. Springer Berlin Heidelberg. https://books.google.com/books?id=ZBf_CAAAQBAJ
- Crasemann, B. (2012). *Atomic Inner-Shell Processes*. Elsevier Science.
<https://books.google.com/books?id=wVR7XHiIg-sC>
- Cutler, J., Chapman, D., Dallin, L., & Lamb, R. (2017). The Brightest Light in Canada: The Canadian Light Source. *Quantum Beam Science*, 1(1). <https://doi.org/10.3390/qubs1010004>
- Diaz, B., Gomez, A., Meyer, B., Duffy, A., Hallin, E., & Kycia, S. (2014). Undulator beamline of the Brockhouse sector at the Canadian Light Source. *Review of Scientific Instruments*, 85(8), 085104. <https://doi.org/10.1063/1.4890815>
- Egami, T., & Billinge, S. J. L. (2003). *Underneath the Bragg Peaks: Structural Analysis of Complex Materials*. Elsevier Science. https://books.google.com/books?id=ek2ymu7_NfgC
- Ethan Merritt. (2010). *X-ray Absorption Edges*. Biomolecular Structure Center at UW.
- Evans, J. (2017). *X-ray Absorption Spectroscopy for the Chemical and Materials Sciences*. Wiley. https://books.google.com/books?id=_p5LDwAAQBAJ
- Evlyukhin, E., Museur, L., Traore, M., Nikitin, S. M., Zerr, A., & Kanaev, A. (2015). Laser-Assisted High-Pressure-Induced Polymerization of 2-(Hydroxyethyl)methacrylate. *The Journal of Physical Chemistry B*, 119(8), 3577–3582. <https://doi.org/10.1021/jp511630p>
- Faraoni, V. (2013). *Special Relativity*. Springer International Publishing.
<https://books.google.com/books?id=NuS9BAAAQBAJ>
- Ferraro, J. R. (2012). *Vibrational Spectroscopy At High External Pressures: The Diamond Anvil Cell*. Elsevier Science. <https://books.google.com/books?id=qDuYOZGe2MYC>

- Fitzpatrick, R. (2008). *Maxwell's Equations and the Principles of Electromagnetism*. Infinity Science Press. <https://books.google.com/books?id=4QaVSxxnyWwC>
- Fodje, M., Mundboth, K., Labiuk, S., Janzen, K., Gorin, J., Spasyuk, D., Colville, S., & Grochulski, P. (2020). Macromolecular crystallography beamlines at the Canadian Light Source: building on success. *Acta Crystallographica Section D*, 76(7), 630–635. <https://doi.org/10.1107/S2059798320007603>
- Garman, E. F., & Weik, M. (2023). Radiation damage to biological macromolecules*. *Current Opinion in Structural Biology*, 82, 102662. <https://doi.org/10.1016/J.SBI.2023.102662>
- Goldberger, D., Evlyukhin, E., Cifligu, P., Wang, Y., & Pravica, M. (2017). Measurement of the Energy and High-Pressure Dependence of X-ray-Induced Decomposition of Crystalline Strontium Oxalate. *The Journal of Physical Chemistry A*, 121(38), 7108–7113. <https://doi.org/10.1021/acs.jpca.7b05604>
- Hammond, C. (2001). *The Basics of Crystallography and Diffraction*. Oxford University Press. <https://books.google.com/books?id=NaGLdNHGvPQC>
- He, B. B. (2018). *Two-dimensional X-ray Diffraction*. Wiley. <https://books.google.com/books?id=G0JbDwAAQBAJ>
- Hughes, S. (2005). *Wave Equation & Electromagnetic Radiation*.
- Jensen, K. L. (2017). *Introduction to the Physics of Electron Emission*. Wiley. <https://books.google.com/books?id=7NA3DwAAQBAJ>
- Katrusiak, A., & McMillan, P. (2004). *High-Pressure Crystallography*. Springer Netherlands. <https://books.google.com/books?id=SAvSBwAAQBAJ>
- Kogut, J. B. (2018). *Special Relativity, Electrodynamics, and General Relativity: From Newton to Einstein*. Elsevier Science. <https://books.google.com/books?id=7UIyDwAAQBAJ>
- Lua Sanchez, A. F., Cifligu, P., Graff, M., Pravica, M., Bhowmik, P. K., Park, C., & Evlyukhin, E. (2023). The high pressure dependence of x-ray induced decomposition of cadmium oxalate. *AIP Advances*, 13(10), 105031. <https://doi.org/10.1063/5.0168449>
- NASA, ESA, & Hustak, L. (2021a, July 2). *Electromagnetic Wave (Light Wave) vs. Mechanical Wave*. Space Telescope Science Institute.
- NASA, ESA, & Hustak, L. (2021b, July 2). *The Electromagnetic Spectrum*. Space Telescope Science Institute.
- National Genomics Education Programme. (n.d.). *RNA*. NHS England.
- National Institute of Standards and Technology. (2004, July). *X-Ray Mass Attenuation Coefficients*. NIST Standard Reference Database 126.
- Pahuja, O. P. (2005). *Solid State Physics*. Laxmi Publications Pvt Limited. <https://books.google.com/books?id=gSSHHubKsLEC>

- Piróth, A., & Sólyom, J. (2007). *Fundamentals of the Physics of Solids: Volume 1: Structure and Dynamics*. Springer Berlin Heidelberg. <https://books.google.com/books?id=zn-se2TKv3QC>
- Prescher, C., & Prakapenka, V. B. (2015). DIOPTAS: a program for reduction of two-dimensional X-ray diffraction data and data exploration. *High Pressure Research*, 35(3), 223–230. <https://doi.org/10.1080/08957959.2015.1059835>
- Rath, S. (2016). *COMPARISON OF CPFEM AND SPECTRAL SOLUTION METHODS IN PREDICTION OF STRAINS NEAR GRAIN BOUNDARIES IN A UNIAXIALLY LOADED OLIGOCRYSTALLINE TENSILE SPECIMEN COMPARISON OF CPFEM AND SPECTRAL SOLUTION METHODS IN PREDICTION OF STRAINS NEAR GRAIN BOUNDARIES IN A UNIAXIALLY LOADED OLIGOCRYSTALLINE TENSILE SPECIMEN*. <https://doi.org/10.13140/RG.2.2.28150.32320>
- Rebollo, F. J. A. (2019). *XRF: X-Ray Fluorescence Spectroscopy*. ALTER TECHNOLOGY.
- Rosenberg, A. (1985). *The Structure of Biological Science*. Cambridge University Press. <https://books.google.com/books?id=faNIAKXQrwQC>
- Sjöstedt, C. (2012). *Iron and aluminium speciation in Swedish freshwaters : Implications for geochemical modelling*.
- Stewart, R. F., & Jensen, L. H. (1967). Redetermination of the crystal structure of uracil. *Acta Crystallographica*, 23(6), 1102–1105. <https://doi.org/10.1107/S0365110X67004360>
- Suryanarayana, C., & Norton, M. G. (2013). *X-Ray Diffraction: A Practical Approach*. Springer US. <https://books.google.com/books?id=RRfrBwAAQBAJ>
- van Bokhoven, J. A., & Lamberti, C. (2016). *X-Ray Absorption and X-Ray Emission Spectroscopy: Theory and Applications* (Issue v. 1). Wiley. <https://books.google.com/books?id=Ho3gCAAAQBAJ>
- West, A. R. (1991). *Solid State Chemistry and Its Applications*. Wiley. <https://books.google.com/books?id=-EKcm5UQaqEC>
- Wiedemann, H. (2013). *Particle Accelerator Physics: Basic Principles and Linear Beam Dynamics*. Springer Berlin Heidelberg. https://books.google.com/books?id=Oo_uCAAAQBAJ
- Willmott, P. (2019). *An Introduction to Synchrotron Radiation: Techniques and Applications*. Wiley. <https://books.google.com/books?id=UV-HDwAAQBAJ>
- XRF RESEARCH, I. (2024). *XRF Spectrum*.

CURRICULUM VITAE

TRIMAAN MALIK

trimaanmalik@gmail.com

EDUCATION

- MS** University of Nevada, Las Vegas: Physics 2024
Thesis: *PHOTOELECTRIC DRIVEN DECOMPOSITION OF URACIL VIA HARD X-RAY IRRADIATION*
- BS** University of Nevada, Las Vegas: Physics 2018
Thesis: *Investigating Stellar Metallicity and Planetary Formation*

RESEARCH EXPERIENCE

Pravica Group

University of Nevada, Las Vegas

2022 to Present

Researcher

Matter at Extreme Conditions

- Performed Raman spectroscopy at high pressure.
- Conducted high pressure X-ray diffraction experiments at synchrotrons.
 - Canadian Light Source (Saskatoon, Saskatchewan, Canada)
 - Advanced Light Source (Berkeley, California, United States)

TEACHING EXPERIENCE

University of Nevada, Las Vegas

Jan 2024 to May 2024

Lab Instructor, Physics

- Taught two classes of undergraduate physics labs for the Spring semester.

PUBLICATIONS

Journal Publications

Canasa, P., King, D., Cifligu, P., Lua Sanchez, A. F., Chen, S. L., Han, H., Malik, T., Billinghamurst, B., Zhao, J., Park, C., Rossman, G. R., Pravica, M., Bhowmik, P. K., & Evlyukhin, E. (2024). "Piezochromic Behavior of 2,4,6-Triphenylpyrylium Tetrachloroferrate," *Small Science*. <https://doi.org/10.1002/smsc.202400106>

Journal Papers in Review

Pravica, M., Cifligu, P., Lua Sanchez, A. F., Malik, T., Appathurai, N., & Diaz Moreno, B. (2024). "A novel means to generate high pressure," *Review of Scientific Instruments*.